COMPUTATIONAL FLUID DYNAMICS STUDY FOR

STABILITY ANALYSIS OF AN UNMANNED

AIRCRAFT MASS SIMULATOR WITH

ROCKET-ASSISTED TAKE-OFF

By

CHRISTOPHER D. TOTTY

Bachelor of Science Mechanical Engineering

Bachelor of Science Aerospace Engineering

Oklahoma State University

Stillwater, OK

2019

Submitted to the Faculty of the
Graduate College of the
Oklahoma State University
in partial fulfillment of
the requirements for
the Degree of
MASTER OF SCIENCE
May, 2022

COMPUTATIONAL FLUID DYNAMICS STUDY FOR

STABILITY ANALYSIS OF AN UNMANNED

AIRCRAFT MASS SIMULATOR WITH

ROCKET-ASSISTED TAKE-OFF

Thesis Approved:

Dr. Kurt Rouser

Thesis Adviser

Dr. Jamey Jacob

Dr. Aaron Alexander

Dr. Ryan Paul

ACKNOWLEDGEMENTS

Throughout this study, I have received incredible support from numerous people. Namely, my advisor Dr. Kurt Rouser provided crucial mentorship and guidance. Dr. Aaron Alexander provided expert instruction and assistance in developing the computational models discussed below. Dr. Ryan Paul provided key insight, critical in analyzing the results of this study. And Dr. Jamey Jacob provided vital acumen, asking the right questions to take this study to a higher level.

In addition to this professional support, many friends and family; especially my father, mother, and sister, have been more supportive than anyone could ask for.

I am forever grateful for these people and many others, and I thank our God above for putting such amazing people in my life and for the ability to contribute to the advancement of this research topic.

Name: CHRISTOPHER D. TOTTY

Date of Degree: MAY, 2022

Title of Study: COMPUTATIONAL FLUID DYNAMICS STUDY FOR STABILITY ANALYSIS OF AN UNMANNED AIRCRAFT MASS SIMULATOR WITH ROCKET-ASSISTED TAKE-OFF

Major Field: MECHANICAL AND AEROSPACE ENGINEERING

Abstract: This paper presents the stability analysis of a high speed unmanned aerial system mass simulator fitted with a rocket-assisted take-off (RATO) system. Flight stability characteristics from rocket ignition to rocket burnout were analyzed using computational fluids dynamics methods to determine the viability of a proposed RATO system as an alternative to other launching methods, as well as traditional take-off. The RATO system used in this analysis is a quad-motor, recoverable design that was developed for testing experimental low-cost solid rocket fuel alternatives. This stability analysis was performed as a critical risk reduction measure for live-fire testing of this RATO system with various propellants. Static longitudinal stability was analyzed, initially using fundamental kinematics, and quickly progressing to the use of computational fluid dynamics to determine the influences of aerodynamic forces. In addition, a proprietary in-house program developed specifically to analyze various launching mechanisms was utilized to estimate the flight trajectory of the mass simulator given the kinematic and computational fluid dynamics analysis results. The analysis has shown that, with the proposed RATO system mounting geometry, the vehicle can achieve and maintain stable flight. This study concludes that the approach laid out within provides a means of adequately analyzing the aerodynamic effects on longitudinal static stability of an unmanned aircraft mass simulator during RATO launch through the use of computational fluid dynamics.

TABLE OF CONTENTS

LIST OF TABLES

LIST OF FIGURES

CHAPTER I

INTRODUCTION

There is currently the need for take-off assistance systems for high-speed unmanned aerial

systems with a gross take-off weight between 50 lbs. and 500 lbs. Examples of aircraft that have

either benefited from or required launch assistance include the Insitu Integrator, Lockheed Martin

Stalker, AeroVironment Raven and Puma, Northrop Grumman FireBee, and even the Kitty Hawk

flown in 1903 by the Wright brothers. [1] There are various methods of launching unmanned

aerial systems of this weight, including traditional rolling runway take-off, pneumatic and

catapult style launching, as well as aero-towing similar to launching manned sailplanes. [1-9]

However, for some users, the reduced infrastructure requirements provided by RATO systems

make them the most desirable launching option. [10] Additionally, certain high-speed unmanned

aerial systems are unable to reach minimum take-off airspeed using alternative methods, making

RATO a necessity. The RQ-2 Pioneer is one of many examples of unmanned aerial systems

utilizing RATO systems as shown in Figure 1. [11]

Figure 1: RQ-2 Pioneer with RATO [11]

The benefits of RATO cover many applications of unmanned aerial systems, including image gathering in emergency response scenarios where time is critical, to weather data collection where unmanned aerial systems are often required to deploy from small ships and boats, and even manned aircraft. The versatility offered by RATO systems comes with its own new set of concerns, namely, cost and stability.

One possible drawback of RATO is that this launching option can greatly impact the stability characteristics of the vehicle. Misalignment of the thrust vectors generated by the solid rocket motors, as well as ignition failure of any of the motors can induce significant pitch, yaw, and roll moments. Additionally, the mounting of any significant mass so far aft of the center of gravity can have a drastic impact on static and dynamic stability of the aircraft. Once the aircraft gains

enough airspeed, the added lift and drag and resulting moments of the RATO system can cause pitching moments that may surpass trim capabilities of the aircraft.

Even after stability concerns are addressed, the viability of RATO systems is still limited by motor cost and availability. [12] Solid rocket motors are far from the most expensive rocket motor options at this scale, but they are still quite costly. [13] Along with this, most manufacturers produce and stock very limited quantities of these motors. A low cost, easily manufactured solid rocket motor is being developed by a team at Oklahoma State University's Aerospace Propulsion and Power lab to mitigate these concerns and make RATO an even more favorable option. [14] The team has built a well-defined understanding of the propulsion performance characteristics of these solid rocket motors through computer aided modeling and conducting static solid rocket motor ground tests. The team is now working towards using these in-house solid rocket motors in the test launch of a high speed unmanned aerial system mass simulator as seen in Figure 2.
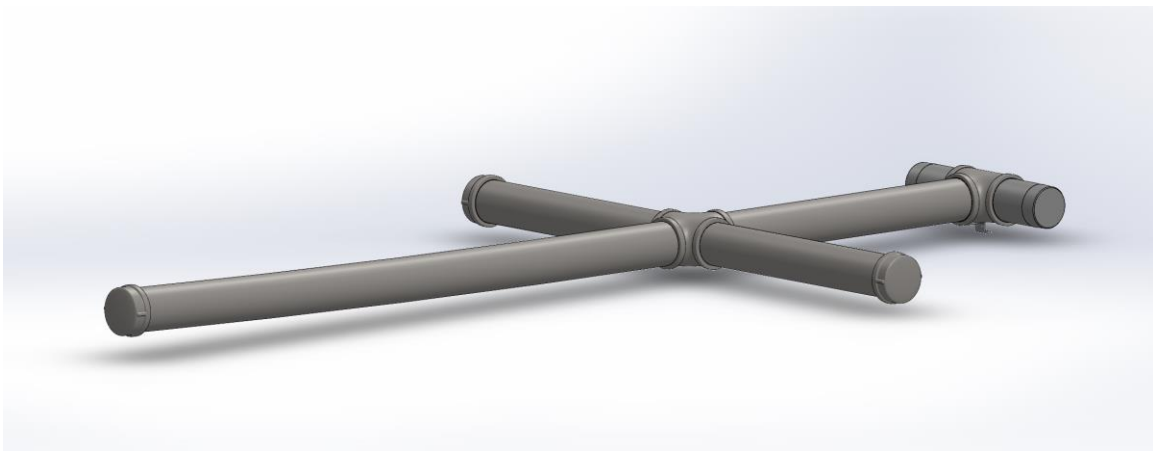
Figure 2: Unmanned Aircraft Mass Simulator
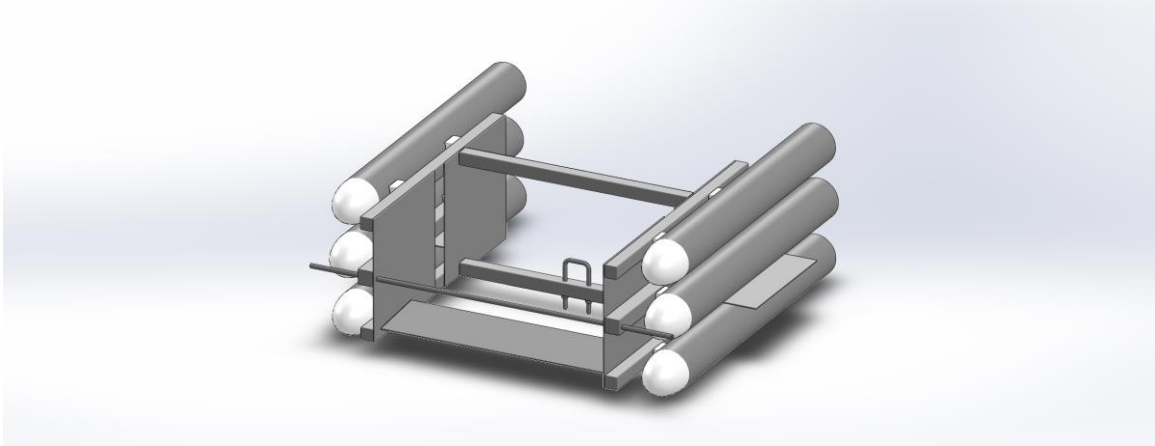
Figure 3: Rocket-Assisted Take-Off System

The notional, aft-mounted RATO system shown in Figure 3 was first fitted with four Cesaroni L2375 rocket motors and two parachute recovery pods. After further testing, the team plans to move forward, replacing the commercial-off-the-shelf solid rocket motors with the in-house low-cost solid rocket motors being developed. The aim of this study is to determine the stability and control characteristics of the given RATO system paired with a 300 lbf mass simulator.

To determine the stability characteristics of the given RATO system and mass simulator, a computational fluid dynamics analysis must be performed. From this analysis, aerodynamic coefficients of the system can be calculated. These coefficients will be are used in an in-house proprietary program to calculate vertical and longitudinal state histories to determine the trajectory and attitude of the mass simulator for a short period after launch. This launch model is used to quantify the feasibility of the proposed RATO system and mass simulator to determine if the system can be safely launched and achieve stable flight.

CHAPTER II

REVIEW OF LITERATURE

SECTION I: SOLID ROCKET MOTORS

Solid rocket motors are the simplest rocket propulsion system available and often used in rocket-assisted take-off systems. [15] In this system fuel and oxidizer are mixed in a chemical composition and cast into solid sections or grains. These grains are then fixed tightly inside the combustion chamber. Once ignited, the fuel and oxidizer combust and form hot gasses which are expelled at the end of the combustion chamber and accelerated through a nozzle. The increase in momentum of this gaseous mass is the cause of rocket thrust, F, as given by

$$F = \frac{\dot{m}_p \times C}{g_c} \hspace{3cm} EQ\ 1$$

Where $\dot{m}_p$ is the mass flow rate of the rocket propellant, C is the effective exhaust velocity, and g_c is the gravitational constant. [16]

Solid rocket motors, in general, are not designed in such a way to be throttled, though methods to do so exist. [17] However, their simplicity and higher mass fraction, the ratio of fuel to system weight, make solid rocket motors the best choice for many applications such as first stage boosters. [18] Though they are relatively simple, for launching vehicles on this scale, they can

still be cost prohibitive. Therefore, a need exists for low cost and easily manufactured solid rocket motors. To demonstrate the effectiveness of motors being developed to meet this need, a mass simulator will be launched via a RATO system utilizing these motors. In order to conduct a safe launch, the flight characteristics of this mass simulator are modeled.

SECTION II: KINEMATICS

Approximate solutions for the mass simulator trajectory can be achieved by solving basic kinematic equations of motion. Two of the generic kinematic equations of motion for a body are defined by

$$v = v_0 + a * t \qquad\qquad EQ\ 3$$

$$\Delta x = v_0 * t + \frac{1}{2} * a * t^2 \qquad\qquad EQ\ 4$$

Where v is the velocity of the body, v_0 is its initial velocity, a is the total acceleration force acting on the body, and t is the time for which this acceleration occurs. [19] When considering pure kinematics, these calculations neglect aerodynamic forces and therefore, are only used to estimate the system's performance. In this idealization, the only forces acting on the mass simulator are the force due to gravity and thrust provided by the solid rocket motors. Considering the launch angle and average thrust, time dependent velocity and angle of attack are calculated. Once this simple analysis was performed a stability analysis was performed considering aerodynamic forces to determine if a similar flight profile can be achieved, or if the system is unstable and likely to diverge from the ideal trajectory.

SECTION III: AERODYNAMIC AND STABILITY THEORY

The objective of this analysis is to determine, as accurately as practical, the longitudinal static stability characteristics and expected trajectory of a high speed unmanned aerial system mass simulator being launched with the proposed RATO system. Understanding of this longitudinal

static stability, or the ability of the system to maintain an equilibrium once established [19], is critical aspect of ensuring launch safety for the unmanned aircraft mass simulator. [20] The kinematic approximations made before are useful for determining a rough solution for the trajectory, but do not factor in the forces induced by moving through the air. In order to account for this, it is critical to understand the basics of aerodynamics. Very generally, aerodynamics is the study of the fluid properties in a region of air. Primarily, this includes fluid velocity, pressure, density, and temperature. Changes in these fluid properties account for all aerodynamic forces on a body in one of two ways; either pressure distribution, p, or shear stress distribution, τ, over the body surface. These two distributions determine the aerodynamic forces and resulting moments. [21] These forces can be broken down in two dimensions to lift, L, and drag, D which, when viewed in two dimensions with respect to the longitudinal direction, result in a moment M, the pitch moment as depicted in Figure 4 below.
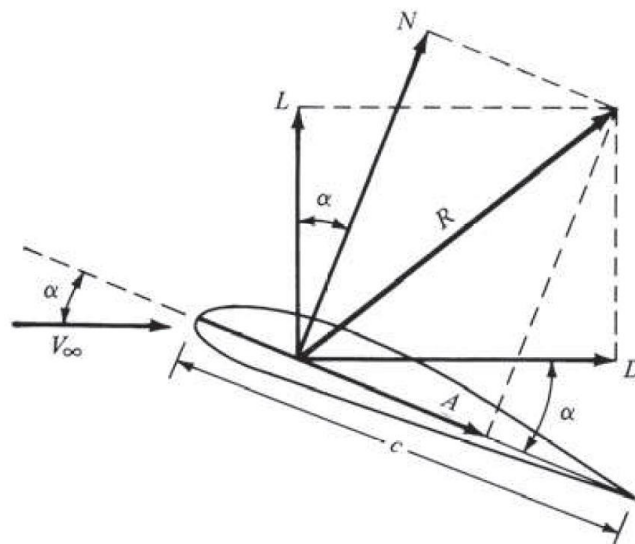

Figure 4: 2-D Schematic of Aerodynamic Forces on an Airfoil [22]

A quality of the freestream that influences the aerodynamic forces on a surface is that of dynamic pressure, which can be defined as

$$q_\infty = \frac{1}{(\frac{2\rho_\infty}{V_\infty^2})} \qquad\qquad \textit{EQ 5}$$

Considering the reference area, S, and reference length of unity, l in a 2-D case the coefficients of

these forces can be defined as

$$C_L = \frac{L}{q_\infty * S} \qquad\qquad \textit{EQ 6}$$

$$C_D = \frac{D}{q_\infty * S} \qquad\qquad \textit{EQ 7}$$

$$C_M = \frac{M}{q_\infty * S * l} \qquad\qquad \textit{EQ 8}$$

Note that these coefficients of lift, drag, and pitching moment; or C_L, C_D, and C_M respectively,

correspond to a three-dimensional body, which for the scope of this paper is sufficient. [22] As

can be seen in Equation 5, as V_∞ approaches 0, the value of q_∞ approaches ∞, causing these

resultant force coefficients to approach 0 at low fluid velocities. These aerodynamic effects apply

to all surfaces of a three-dimensional body and, along with the body's mass properties and

propulsion systems, determine whether the body can reach and maintain stable motion.

Stability is generally defined as an object or system's ability to return to its equilibrium state. [23]

The focus in this analysis is on longitudinal static stability. To be considered longitudinally

statically stable, the features of a body will generate a pitching moment opposite that of any

disturbance. If the body begins to pitch up, the lift and drag distributions about the body will

result in a downward pitching moment. This is demonstrated by EQ 9, the longitudinal static

stability criterion. [24]

$$\frac{\partial C_{M_{cg}}}{\partial \alpha} = C_{M_\alpha} < 0 \qquad\qquad EQ\ 9$$

Additionally, in order to trim at positive angles of attack, the C_{M_α} plot must have a positive

intercept, or $C_{M_0} > 0$. [25]

Solving for the lift and drag forces about a circular cylinder produces an oscillation in the

resulting force values with respect to time. This is due to a mechanism referred to as vortex

shedding. [26] It is assumed that the time step of this oscillation relative to the time step of

interest will minimize the effect of vortex shedding on the results of this study, to the point that

these effects can be neglected.

These values above can be solved by hand for very simple geometries; however, for complex

systems such as this mass simulator and RATO system, the equations become far too complicated

to be solved directly. In cases such as this, computational methods are used.

SECTION IV: COMPUTATIONAL FLUID DYNAMICS

Computational fluid dynamic analysis is the art of replacing the governing partial differential

equations of fluid flow with numbers and advancing these numbers in space and/or time to obtain

a final numerical description of the complete flow field of interest. [27] Generally, computational

fluid dynamics codes are based off of the Navier-Stokes equations which completely describe the

aerodynamics of a fluid. [27] Solving these equations in discrete volumes throughout the flow

field allows very accurate modeling of the flow in and around complex geometries such as the

mass simulator and RATO system analyzed in this study.

Computational fluid dynamics studies are often used to estimate the aerodynamic forces and

coefficients acting on an aircraft. [28-29] These results are generally then plugged into an aircraft

modeling software or used to directly solve for the stability derivatives of a given system. [30]

[31-32] Significant amounts of time can be spent developing an extremely high-fidelity computational fluid dynamics model; however, it is important to note that this analysis is not intended to be a rigorous computational fluid dynamics study, but rather an analysis that is accurate enough for all practical applications, this accuracy will be demonstrated through a sensitivity study of the various parameters.

Many computational fluid dynamics software's are available, with two of the more common offerings being Simcenter Star-CCM+ and ANSYS Fluent. In this case Simcenter Star CCM+ was used due to availability. While these two programs do vary, in prior studies Star CCM+ has been shown to perform very similarly and yield very similar results to those of ANSYS Fluent. [33] As with all computational modeling programs though, the viability of each simulation is extremely dependent on the specific system and the end user setup of said simulation. One widely accepted method of verifying a computational fluid dynamics simulation and solution is to compare it to a well-known aerodynamics problem, in this case, 2-D uniform flow around a cylinder. [34-35] This method of verification is conducted in this study to ensure that the setup of the simulation adequately models the system for the purpose of obtaining aerodynamic forces and coefficients for use in determining system stability.

Within Star CCM+ there are two solvers that are used independently to model the turbulent boundary layer near the surfaces of bodies in the flow, where fluid characteristics change drastically within a very small region. [36] The factor used to determine which model is used is Wall Y+ which refers to the position within the turbulent boundary layer relative to the shear viscosity and kinematic viscosity as defined below

$$y^+ = \frac{y * u_t}{v} \qquad\qquad EQ\ 11$$

Where u_t is the shear velocity, given by

$$u_t = \sqrt{\frac{\tau_w}{\rho}} \qquad\qquad \textit{EQ 12}$$

Where v is the fluid velocity, τ_w is the shear in the fluid flow, and ρ is the fluid density. Ideally, the turbulent boundary layer would be fully simulated, but the mesh density required to achieve this is much higher, which increases computational demand and requires more end-user setup time.

SECTION V: PREVIOUS WORK ON RATO

The use of RATO to launch aircraft is not new. However, information on this topic in the public domain is often limited. [37-38] Research has been done to address certain aspects of RATO and specifically its use with unmanned aerial systems. These studies have shown that, in general, once a statically stable unmanned aerial system has gained enough airspeed to have control authority, an onboard autopilot system can achieve and maintain the desired flight path. [39] Previous studies have emphasized that one of the most critical factors in a safe launch is the location of the longitudinal center of gravity with the RATO system installed, and that the implications that can have on longitudinal stability are significant. [40] In previous studies CFD has been successfully used to analyze the impact of varying side winds and external pitching moments due to propulsion system thrust interactions as it applies to a vehicles launch dynamics. [41-42] There is still a need for understanding the launch characteristics of a simulated mass being launched with an attached RATO system. It is the aim of this study to utilize proven methods such as those aforementioned to address this need by analyzing the longitudinal static stability of said system and simulate the launch trajectory.

CHAPTER III

METHODOLOGY

SECTION I: MASS SIMULATOR

The mass simulator and RATO system being designed by a team at Oklahoma State University's
Aerospace Propulsion and Power lab is based on an approximate 300 lbm gross take-off weight
and is currently scalable up to 350 lbm gross take-off weight. As can be seen in Figure 2 & 5, the
mass simulator is configured in such a way to model generic high speed unmanned aerial systems
of the 50 lbm to 500 lbm gross take-off weight range. The mass simulator is constructed of
heavy-duty steel pipe and the RATO system is designed to be as light as practical to minimize the
shift in center of gravity associated with the installation of the system onto the mass simulator.
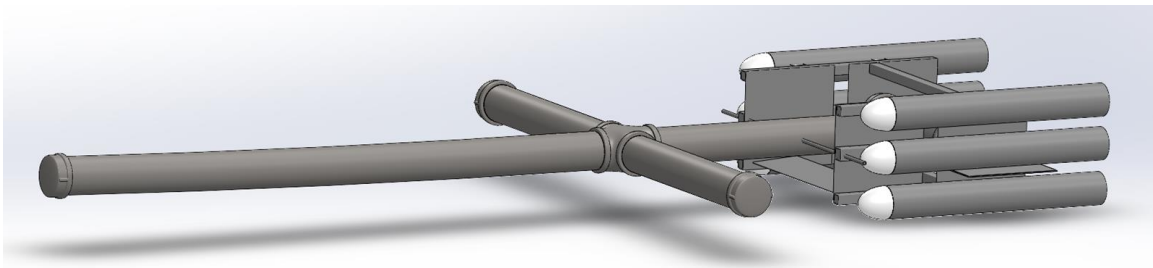
Figure 5: Mass Simulator and RATO System Assembly

With the gross take-off weights being considered, steel pipe was used to not only reach those
weights, but to increase the likelihood of components being reusable for subsequent test launches,

as well as a cost reduction measure. The fuselage, wings, and tail are all modeled with four-inch nominal steel pipe that has a 4.5 in. outside diameter. that is threaded together using the required fittings. The center of gravity, with the RATO system installed is located 5.6 in. behind the leading edge of the wing.

As shown in Figure 3 & 5, the RATO system is comprised of six tubes attached to a bracket assembly. This assembly was constructed using high strength structural fiberglass to reduce weight as much as possible while remaining more affordable than carbon fiber alternatives. The tubes on the four corners of the six-tube system are the housings for the rocket motors. The inner two tubes are intended to house parachute recovery systems which will aid in separation as well as recovery of the RATO system with the goal of reusability. It is important to note that, while it is extremely close, the model shown is not a one for one model of every minute feature of the system.

Given the scale and complexity of the mass simulator, certain assumptions have been made to reduce computational time. This is done to reduce the number of cells required to model the system and in turn reduce the computational resources needed to run each CFD simulation. Namely, relatively small features such as fasteners and any excess epoxy at joints in the RATO bracket have been assumed negligible, as the focus of the CFD analysis is on the bulk forces. Similarly, small portions of thread protruding from the pipe fittings are also neglected and a smooth interface is assumed. Additionally, assumptions about the rocket motors themselves have been made. Rather than modeling the exact thrust profile of the rockets, a step function was written for the transient thrust value as the periods of time between ignition, ramp up, nominal thrust, and burnout are all quite small relative to the overall burn time. These values were provided by the team designing the RATO system. Ideally, these transient values would be accounted for, but given the neutral burn profile of the rockets and the time scale on which these

changes occur, these averaged values provide a very accurate approximation of the force applied to the body during launch by the rocket motors.

SECTION II: COMPUTATIONAL FLUID DYNAMICS

The setup within Simcenter Star CCM+ is critical. This setup determines the accuracy and repeatability of the CFD results calculated. To model the system as accurately as practical, the physics values were tailored to this specific case. The fluid volume was defined as 32.8 ft from the top, bottom, left, and right sides of the mass simulator with the inlet 65.6 ft in front of the body and the outlet 98.4 ft behind as shown in Figure 6 below.
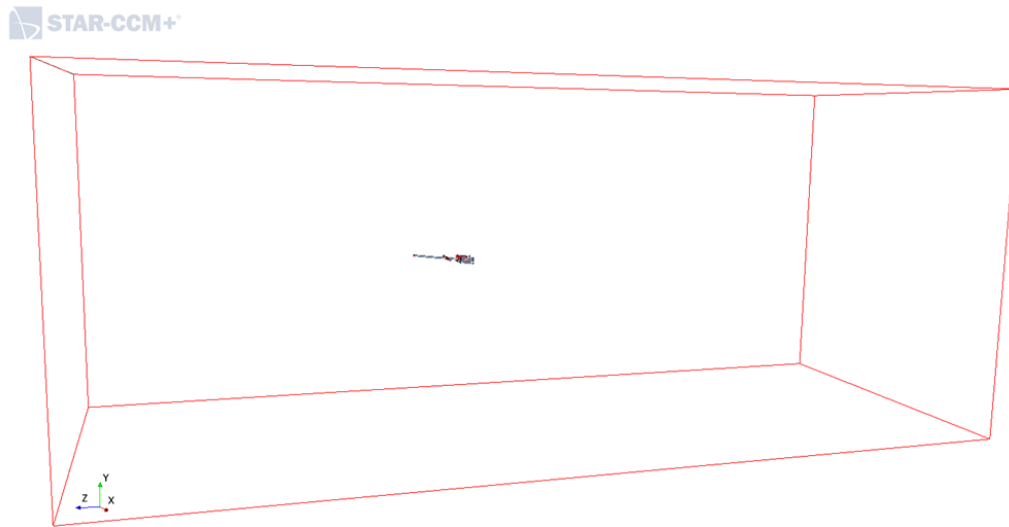
Figure 6: Flow Domain

The inlet was set as a velocity inlet with the freestream velocity being 58.667 ft/s and the static temperature being 90°F, given that the planned launch will take place on an Oklahoma summer day. The walls of the fluid volume were set as slip interfaces. In this instance the surface re-mesher, polyhedral mesher and prism layer meshers were used. Physics models selected include all wall Y+ treatment, K-Omega turbulence model, Reynolds-Averaged Navier-Stokes equations, steady flow, coupled energy, ideal gas assumptions, gradient modeling, and three-dimensional

modeling. The mesh was generated with a 9.84 in. base size. A target surface size of 0.0984 in. or 1% of base was selected and is equal to the minimum surface size set. The surface curvature was defined with 36 points per circle. Surface proximity settings were a 0.0 ft search floor with 2 points in gap. The default growth rate of 1.3 was used. In order to model the viscous sublayer of the turbulent boundary layer, the prism layer geometry was iteratively refined to reach a wall y+ lower than one. The resulting prism layer geometry consisted of 10 layers and a prism layer total thickness of 0.1114 in with a 1.75 stretch factor. A volumetric growth rate of 1.2, the default, and a maximum cell size of 98.4 in., or 1000% the base cell size was selected. Core mesh optimization was allowed to run for one cycle and 0.4 was set as the cell quality threshold. Custom controls were used on the inlet outlet and walls of the fluid volume, as well as the rocket tubes, bracket, and pipe fittings, given their differing geometry. For the rocket tubes and bracket, this included a target surface size of 0.2460 in. or 2.5% of base. The custom controls on the pipe fittings included a target surface size of 0.0492 in. or 0.5% of base, as well as 12 prism layers with a total thickness of 0.1115 in. or 1.133% of the base cell size. The inlet and outlet were assigned a target surface size of 7.874 in. or 80% of the base size. The walls were given a target surface size of 19.685 in. or 200% of base, as well as 1 prism layer with a total thickness of 2.461 in. or 25% of base. Wake refinement was used on the entire body of the mass simulator for 6.56 ft in the [0, 0, -1] direction with a spread angle of 5.0 degrees, isotropic size of 0.0820 in. or 10% of base and 1.3 as the surface growth rate. A stopping criteria of 2001 iterations was used to ensure a sufficient number of iterations to reach quasi-convergence on a solution. Note that the use of an unsteady solver was considered to account for the vortex shedding frequencies generated by the cylindrical bodies involved, but a steady solver was opted for given the significantly increased demand of an unsteady case for each point on the alpha sweep discussed below. The aerodynamic coefficients were then calculated based on mean solution values for 1000 iterations after quasi-convergence is reached. Figures 7-13 show the resulting mesh geometry and flow velocity, wall

y+, and pressure scenes for this simulation setup, which will be referred to as Case A.
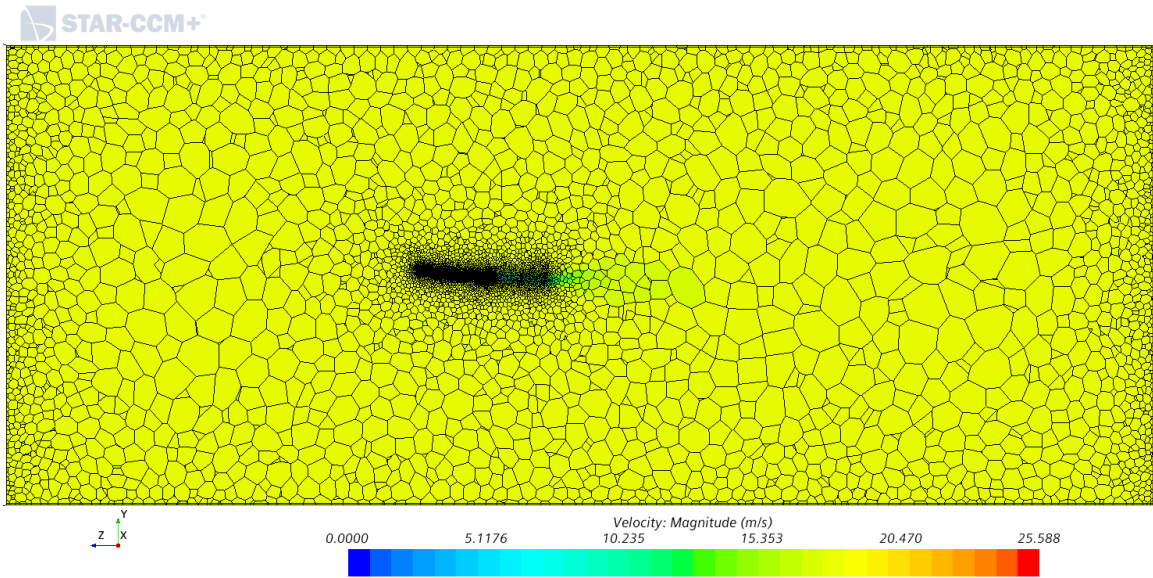
Figure 7: Case A Mesh Topology for Entire Volume
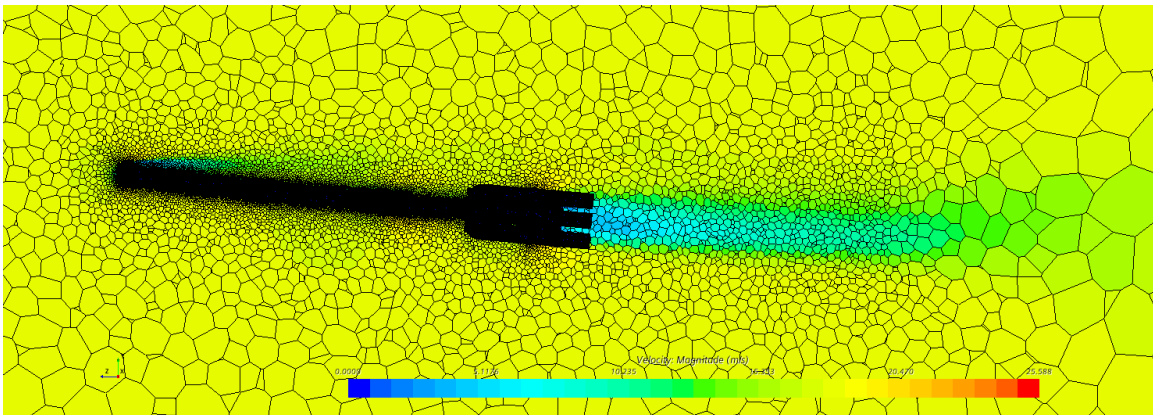
Figure 8: Case A Mesh Topology Near Mass Simulator
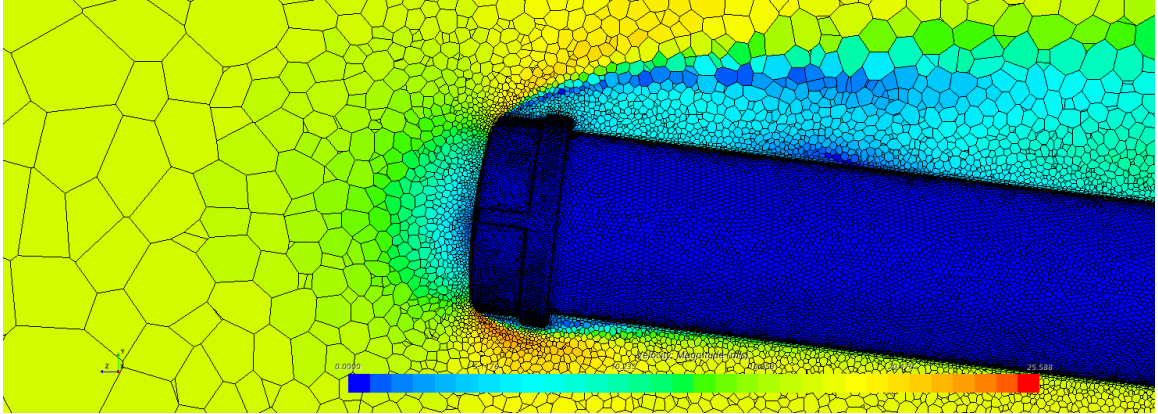
Figure 9: Case A Mesh Topology Near the Nose
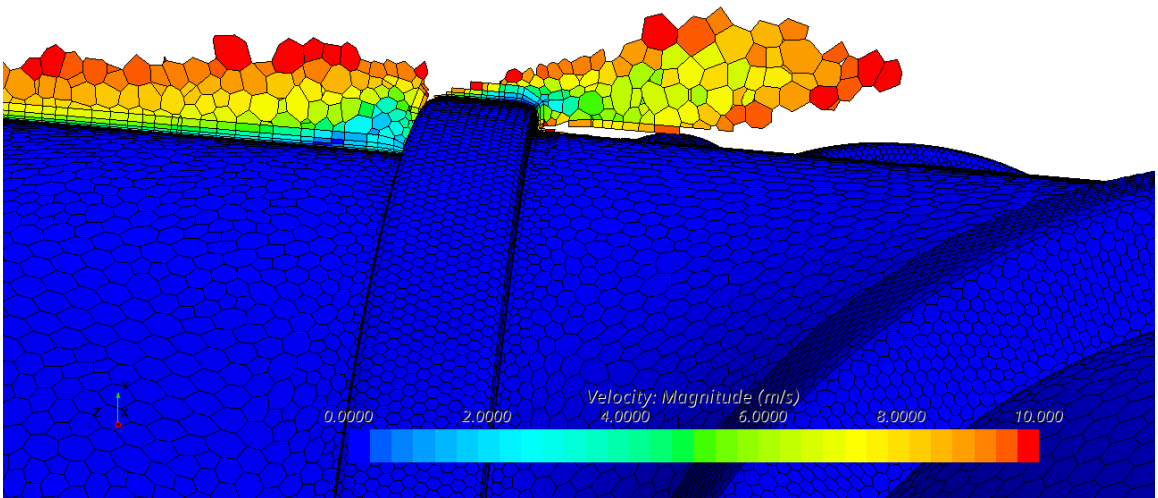
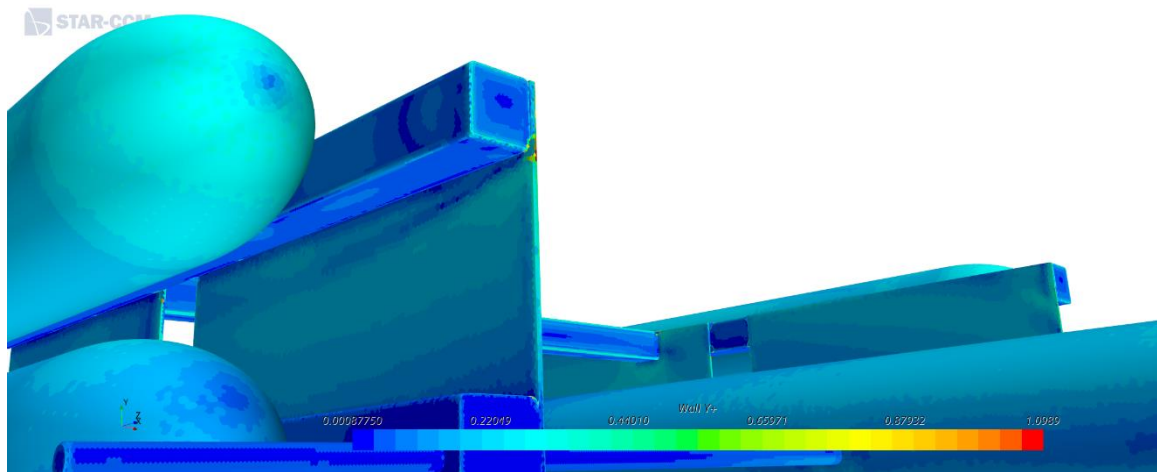*Figure 10: Case A Mesh Prism Layer Topology*
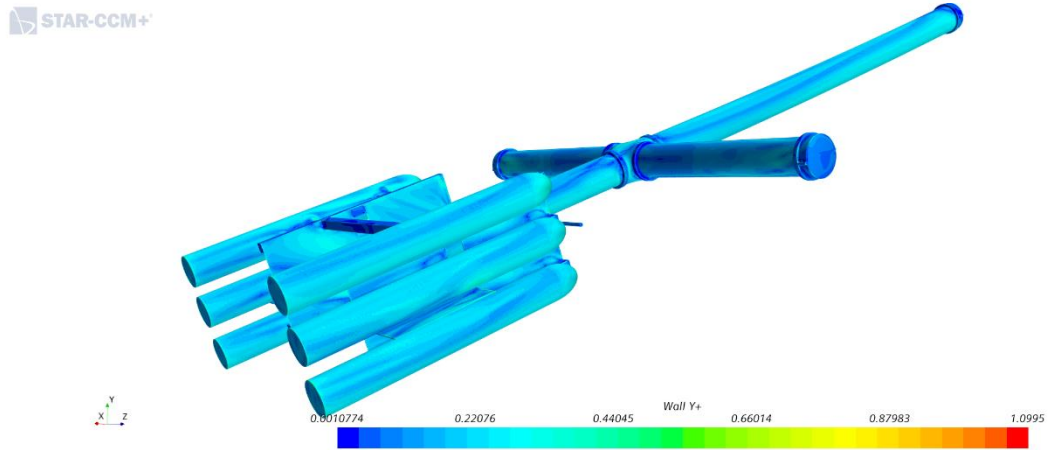
Figure 11: Case A Wall y+

Figure 12: Case A Wall y+ on RATO Bracket Surfaces

Two additional mesh geometries were run with similar physics values to verify the results generated using the mesh in Case A. In Case B, all values were held constant, but with 40 prism layers rather than 10, and a stretching factor of 1.2 instead of 1.75, which resulted in a much higher prism layer density as shown in Figures 13-14 below.
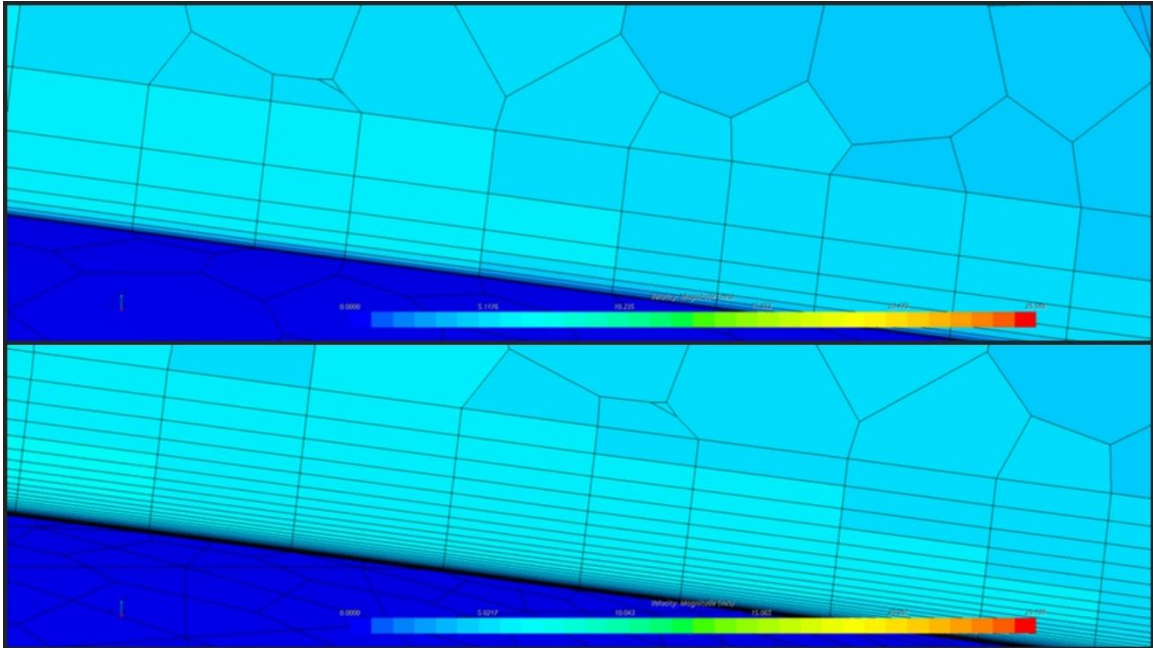
Figure 13:Comparison of Case A (Top) & B (Bottom) Mesh Topology at 5° α, Top Surface of

Front Fuselage

Shown in Figures 14-15 are the residuals, which indicate local imbalances in variables that are bound by laws of conservation, such as energy. These residuals are measured at each iteration and are plotted on a log scale. A large drop in residuals would indicate a step towards a solution away from an initial condition, a small drop would indicate a solution that is very close to the initial conditions. Additionally, if these residuals converge at a certain value and remain nearly constant for many iterations, this indicates the stability of the given solution. The residuals of Case B would at initial glance indicate much better convergence than those in Case B; however, the resulting solution is not that different.
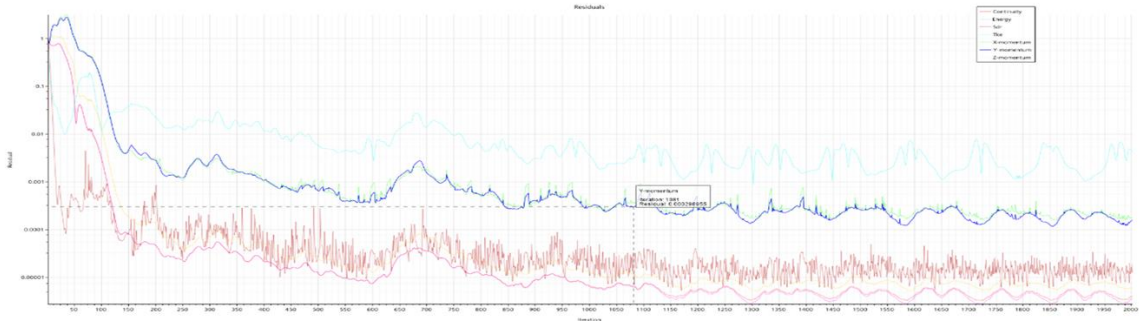
Figure 14: Case A Residuals
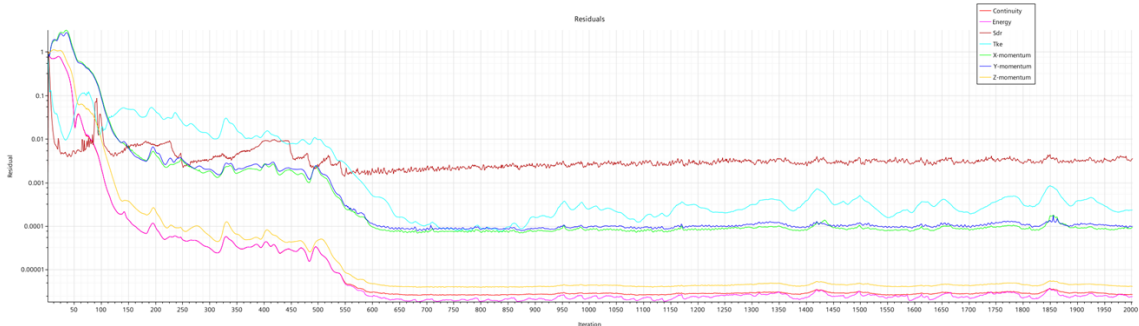
Figure 15: Case B Residuals

Despite what the residuals would initially indicate, the results from the two cases are very similar, except for C_L; however, this is to be expected given the low magnitudes of C_L being considered. Table 1 shows the percent differences, or the differences over the averages of all three coefficients from Case A and Case B.

Table 1: Case A & B Comparison of Aerodynamic Coefficients

Coefficient	Percent Difference, Case A & B
C_L	7.76 %
C_D	0.24 %
C_M	0.09 %

Case A was again compared with Case C, in which all values were held constant, with the addition of adaptive mesh refinement, a system which splits cells based on the gradient of a parameter from one cell to the next. In this case, turbulent kinetic energy was selected given that it naturally varies quite significantly within flow that is interacting with the body and remains constant in freestream flow that is undisturbed. Figures 16-18 display the resulting mesh geometry and flow velocity scenes, and residuals generated using Case C at 5° α.
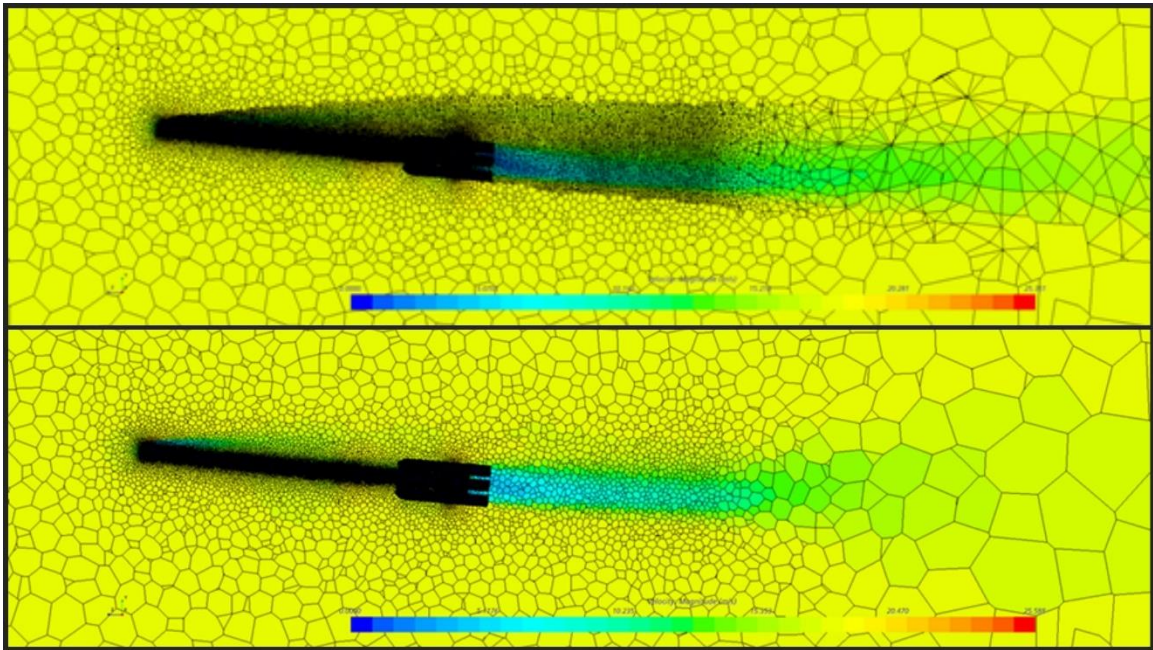
Figure 16: Comparison of Case C (Top) & A (Bottom) Mesh Topology at 5° α
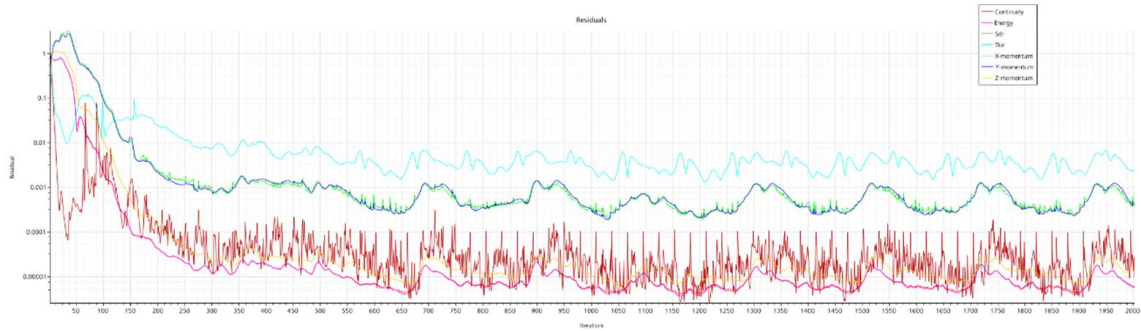
Figure 17: Case A Residuals
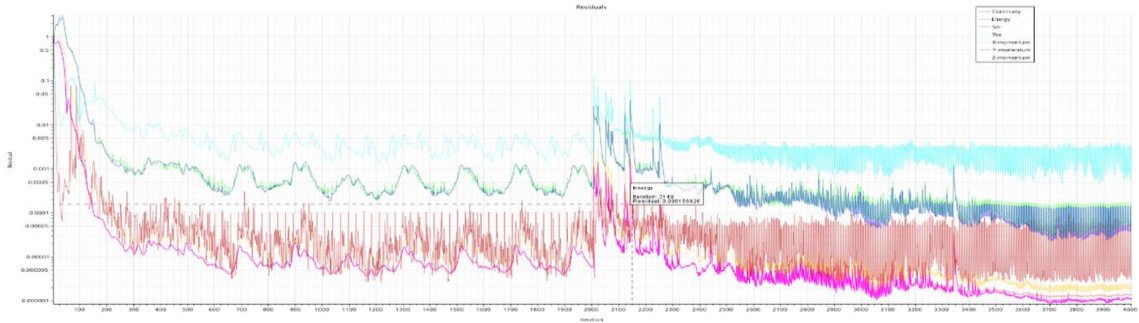
Figure 18: Case C Residuals

As seen in the example of mesh topography for Case C, there are approximately 28,000,000 cells, as opposed to the 16,000,000 generated in Case A, with the majority of these additional cells in the areas of flow interactions in close proximity to the mass simulator. The resulting mesh produced residuals that oscillated much more frequently, but with very similar magnitude to those of Case A. However, the percent differences of C_L and C_M, are still quite small, less than 10%.

Table 2: Case A & C Comparison of Aerodynamic Coefficients

Coefficient	Percent Difference, Case A & C
C_L	13.03 %
C_D	7.12 %
C_M	9.81 %

SECTION III: 2-D VERIFICATION

Lastly, the mesh geometry in Case A was applied to a 2-D flow simulation on a cross section of 4-inch nominal pipe, which has a 4.5 inch outside diameter, equal to that of the mass simulator. Using Figure 26 [44] the approximate drag of the cylinder is found and compared to the drag calculated by the 2-D simulation, shown in Figures 19-23.
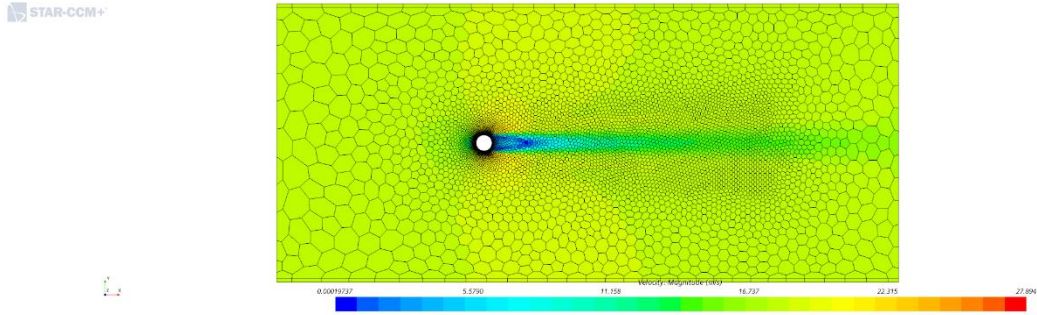
Figure 19: 2-D Case Mesh Topology for Entire Volume
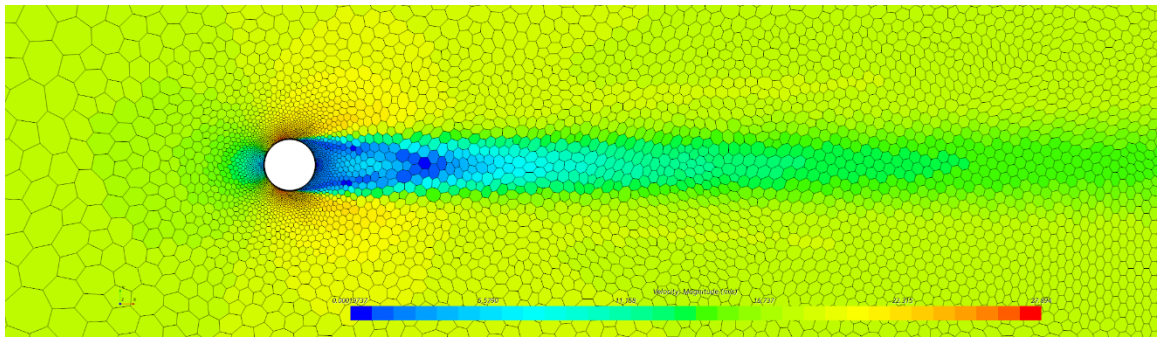
Figure 20: 2-D Case Mesh Topology Near the Cylinder
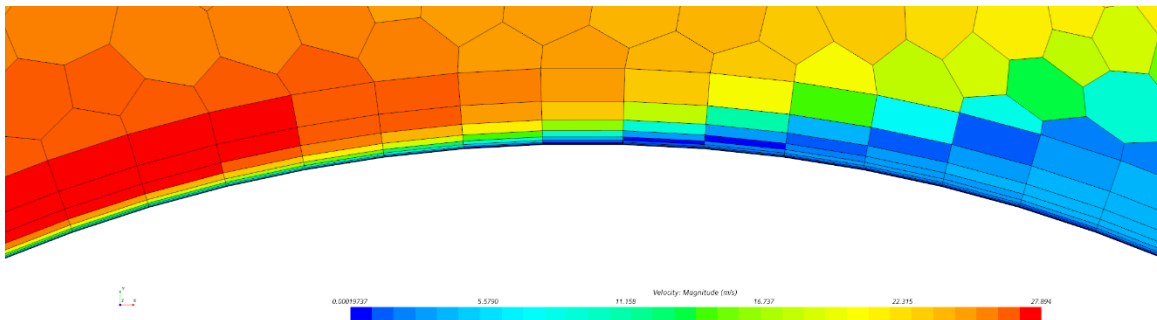
Figure 21: 2-D Case Mesh Prism Layer Topology
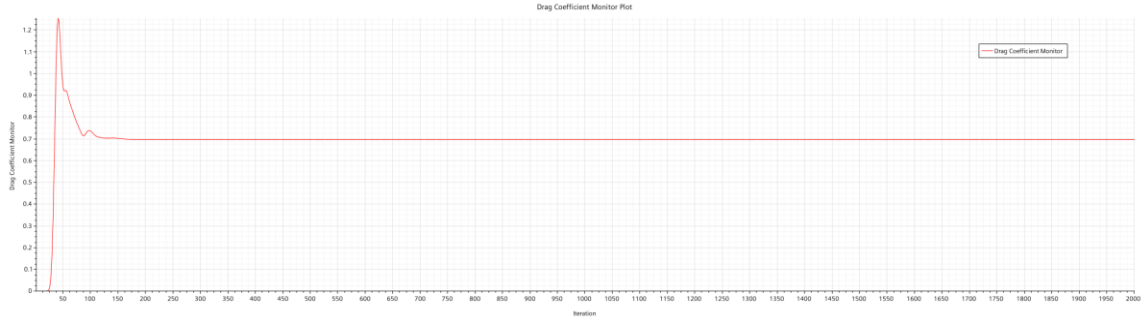
Figure 22: 2-D Case C$_D$
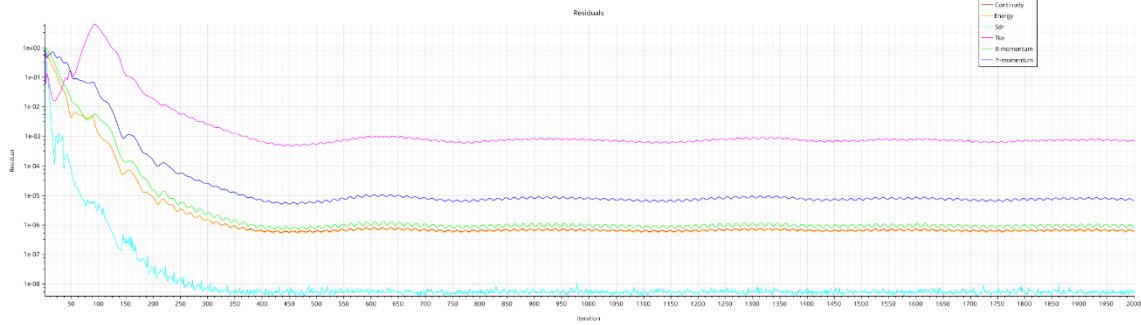
Figure 23: 2-D Case Residuals

The 2-D Case utilizing the mesh settings from Case A yielded residuals that indicate stable

convergence on a solution and a $C_D = 0.66$, which is right within the range of 0.6-0.7 that is

expected from Figure 24 [44], which shows empirical data from wind tunnel tests of 2-D cylinder

drag coefficients at a range of Reynolds numbers, given that $Re \approx 135,000$ in this study.
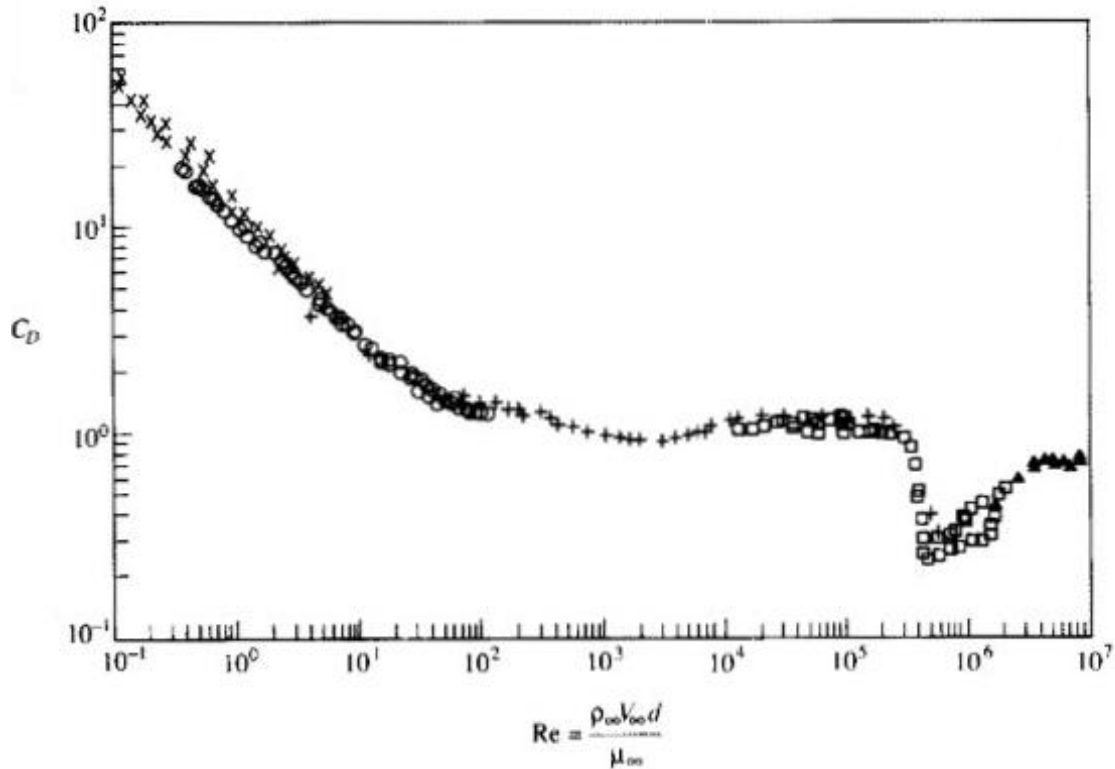
Figure 24: C_D of 2-D Cylinder at Range of Re [44]

Given that the 2-D results using the mesh topography from Case A yielded results very close to what is shown in empirical data, and the relatively small percent differences demonstrated using vastly denser mesh topographies, the mesh topography of Case A is used at multiple α to generate a drag polar for use in the launch simulator.

The launch simulator is an in-house program used to model the expected trajectory and attitude of the aircraft within 3 seconds of launch. This is the period leading up to the point when the rocket-assisted take-off assembly will burn out and separate from the mass simulator with the assistance of the deployable parachutes. This program utilizes aerodynamic differential equations of motion of the system and implements an ordinary differential equations solver to solve for the vertical

and horizontal components of position and velocity. The simulator operates off of the assumption that the system being considered processes static longitudinal stability.

Factors accounted for in this simulator include wind, launch inclination angle, height above ground, aircraft mass and drag polar. Additionally, the simulator considers thrust profile, relative direction, and burn time. The outputs of the simulator include state histories of the aircraft in the horizontal and vertical directions, as well as longitudinal attitude with respect to time.

CHAPTER IV

FINDINGS

SECTION I: AERODYNAMIC FORCE COEFFICIENTS

Utilizing the parameters detailed above, simulations generated results that quasi-converged to

yield lift, drag, and pitch moment coefficients of the mass simulator. The term quasi-convergence

is used due to the residuals not fully converging, but rather oscillating about a value. As shown

above, further refinement yielded fairly low percent differences in the coefficients; therefore,

Case A was used to solve for the coefficients of lift, drag, and pitch moments. The mean values

were calculated for the last 1000 iterations of each 2000 iteration run. These values are recorded

below in Table 1.

Table 3: Aerodynamic Coefficients

α °	C_L	C_D	C_M
-15	-0.17405	0.298684	0.012059
-12.5	-0.14622	0.281361	0.010312
-10	-0.10839	0.260126	0.007633
-7.5	-0.07973	0.241659	0.005709
-5	-0.05044	0.224868	0.00398
-2.5	-0.0534	0.214627	0.003444
0	-0.02236	0.21404	0.001106
2.5	0.014008	0.220851	-0.00157
5	0.052443	0.231865	-0.00426
7.5	0.087122	0.246098	-0.0062
10	0.105349	0.26568	-0.00744
12.5	0.116834	0.27862	-0.00803
15	0.135909	0.290433	-0.00893
17.5	0.163649	0.304592	-0.00993
20	0.196147	0.321498	-0.01143

Plotting each of these values results in the following. As should be expected, $C_L = 0$ at $\alpha = 0$; however, there is notable nonlinearity in the C_L plot at values very near $\alpha = 0$, this is expected due to the low values of C_L, resulting from a mass simulator that has no lifting surfaces in its design. Because of these low values of C_L, slight differences in the output appear quite large. It is critical to note that, given such small values of C_L, the impact of these small variances will be negligible on the overall trajectory of the mass simulator, as shown in a sensitivity study below.
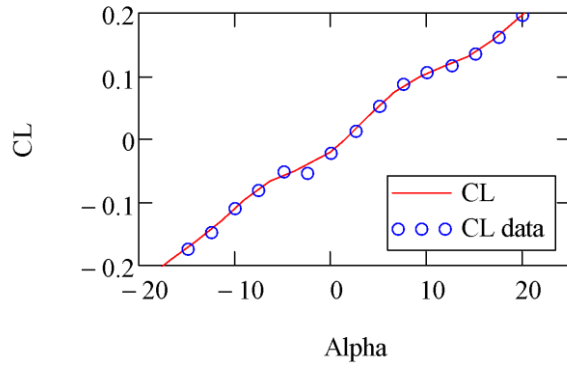
Figure 25: C_L with Respect to Angle of Attack, α
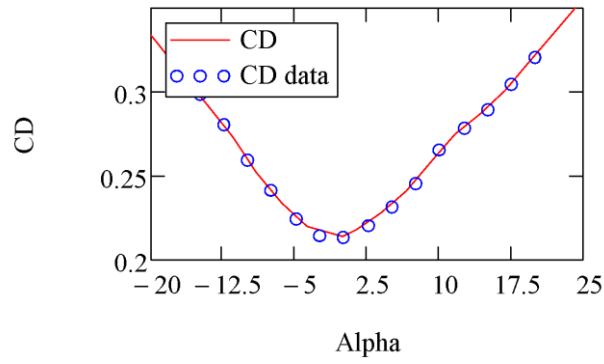
Figure 26: C_D with Respect to Angle of Attack, α
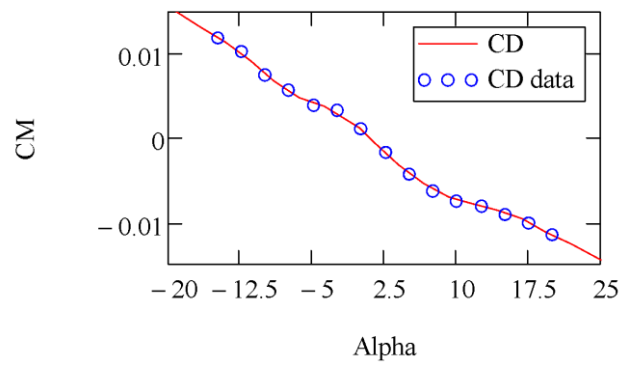
Figure 27: C_M with Respect to Angle of Attack, α
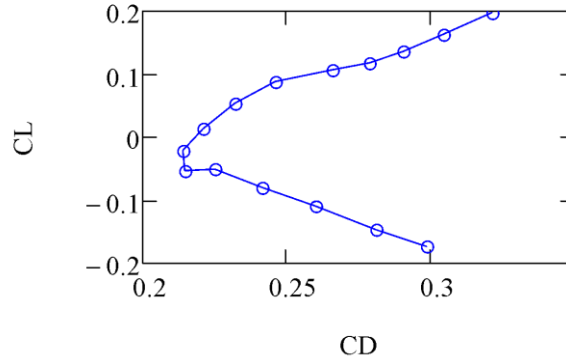
Figure 28: C_L with Respect to C_D

As for C_D, results match what would be expected for such a system based on empirical data for other objects. [23] Lastly, C_M results match what would be expected for this system, given that the majority of drag inducing surfaces of the mass simulator are aft of the center of gravity, inducing a restoring pitching moment when perturbed. In Figure 27 it can be seen that the static stability criterion shown in EQ 9 is met, given the negative slope and positive intercept. Therefore, these results can be used as inputs in the launch simulator, as they meet the assumption of longitudinal static stability.

SECTION II: STATE HISTORIES

Given the aerodynamic coefficients in Table 1, the outputs of the launch simulator are shown in Figures 29-33 In these figures, it can be seen that the simulation using the aerodynamic data very closely matches the values found in the kinematic analysis. This similarity is likely due to the fairly low value of lift, as well as the low values of force due aerodynamic drag at these launch velocities, relative to the force provided by the rocket thrust. For example, the drag force reported at $t = 2\ s$ is $D = 195.54\ lbf$, compared to the average thrust value of $F = 2300\ lbf$; so, as shown, the inclusion of drag forces has a relatively small impact on the state histories during this time interval.
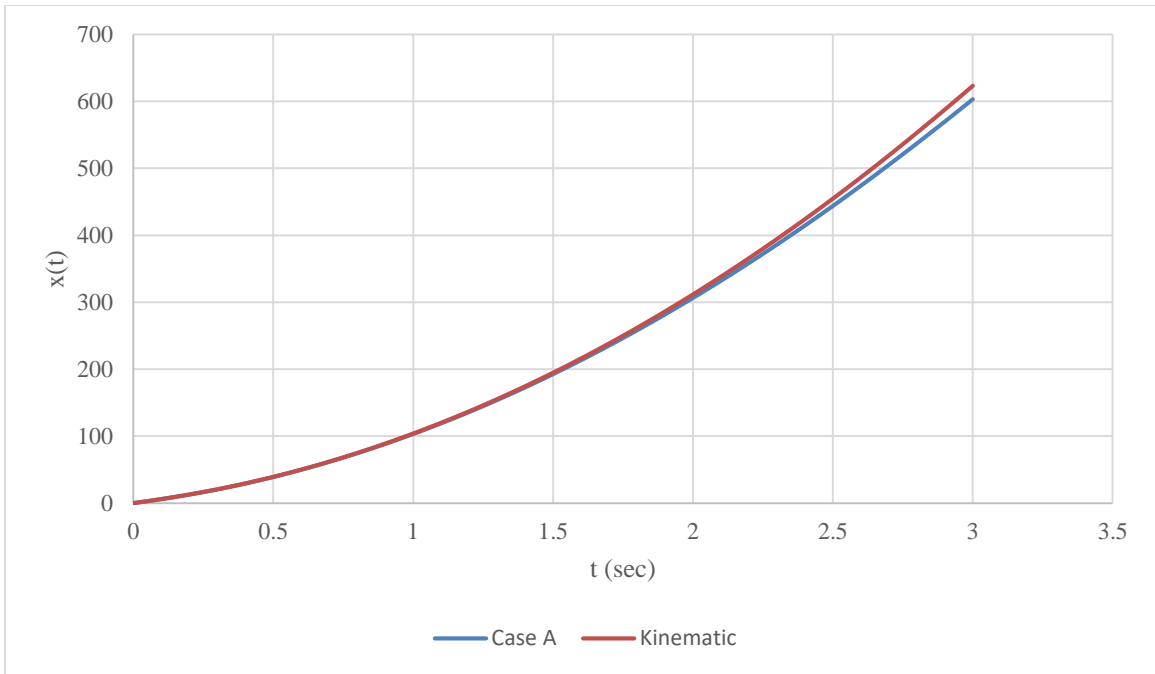
Figure 29: Case A Trajectory x(t) Compared to Kinematic Solution
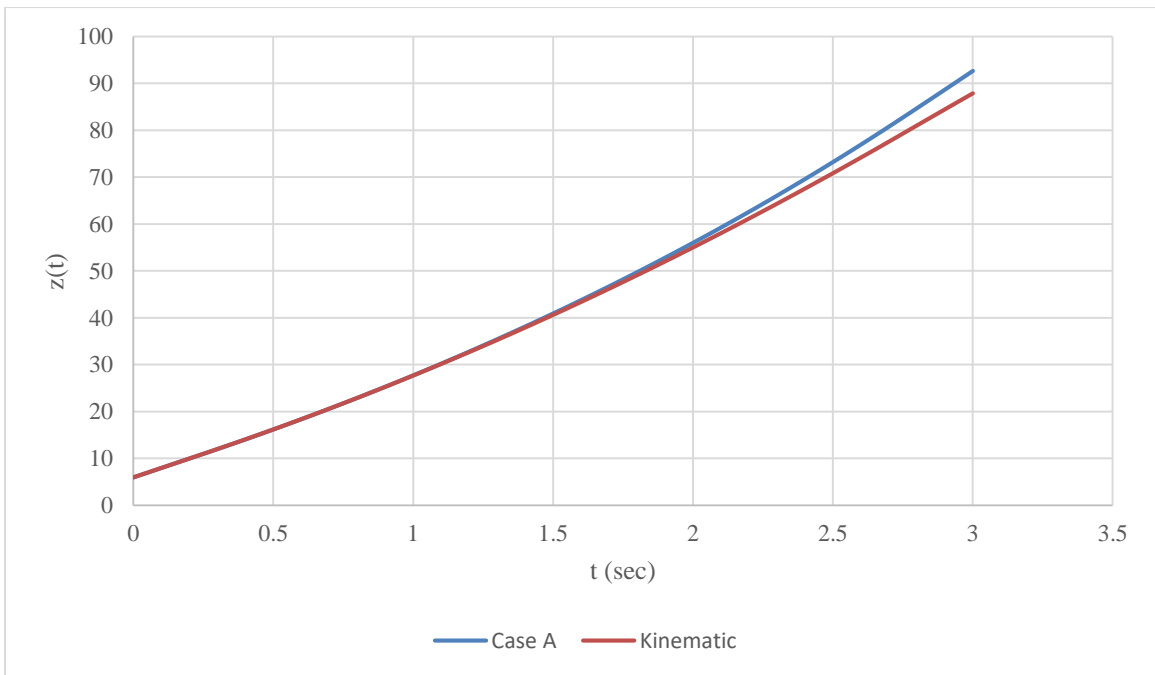
Figure 30: Case A Trajectory z(t) Compared to Kinematic Solution
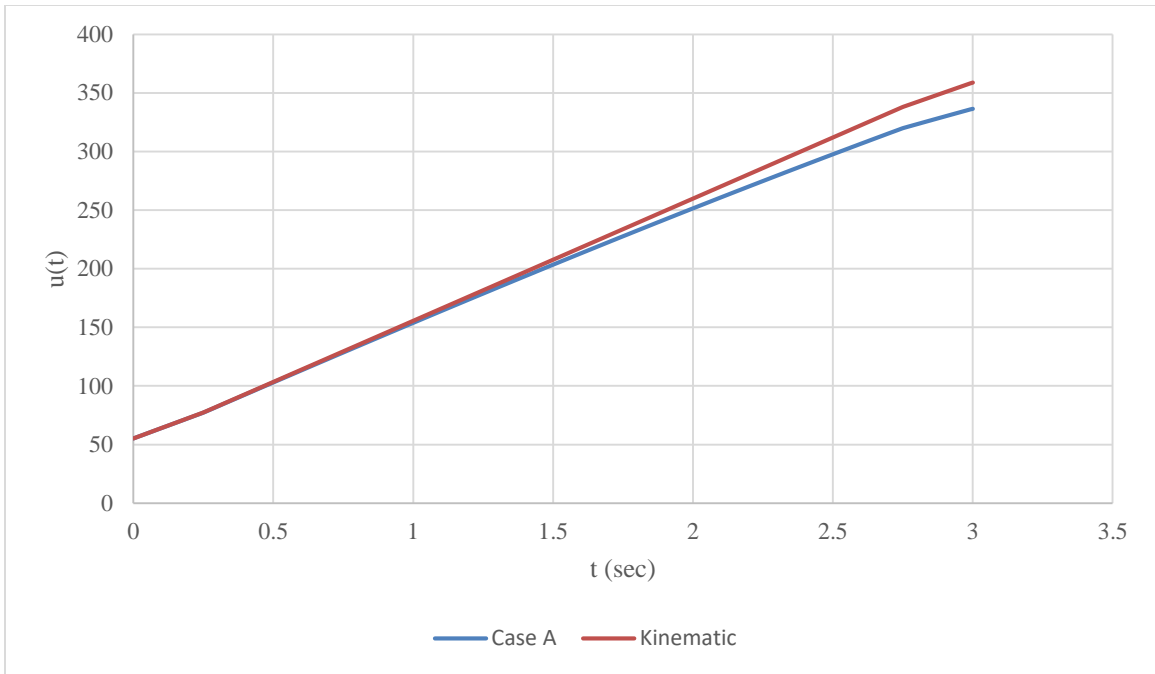
Figure 31: Case A Trajectory u(t) Compared to Kinematic Solution
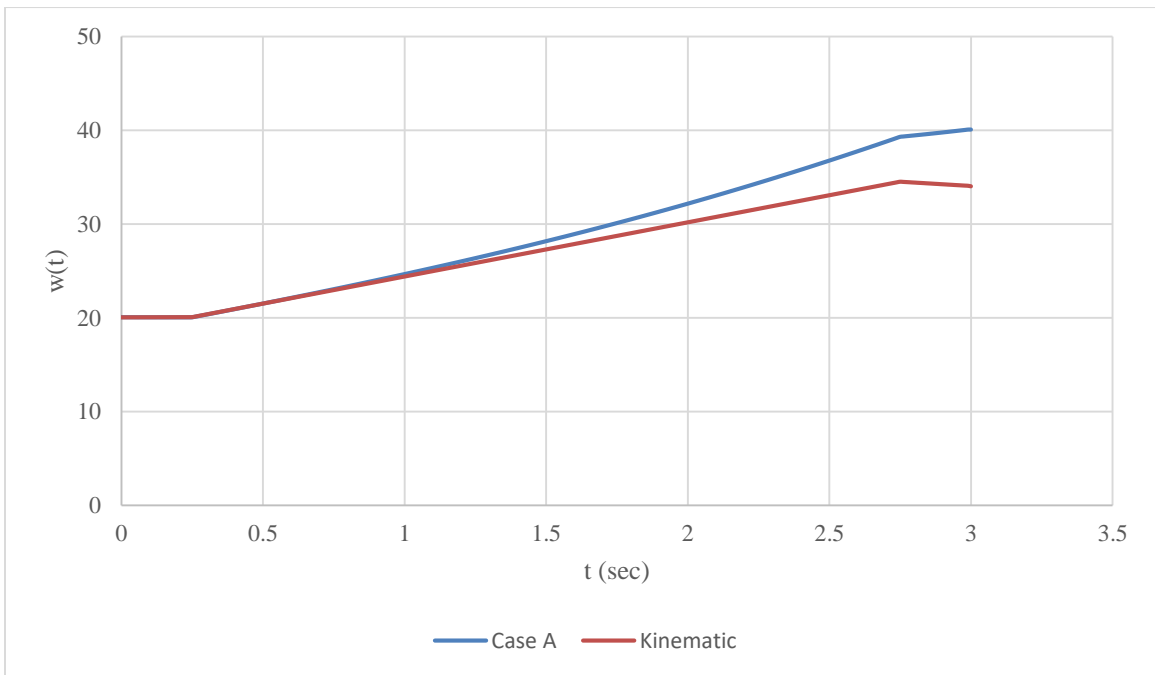
Figure 32: Case A Trajectory w(t) Compared to Kinematic Solution
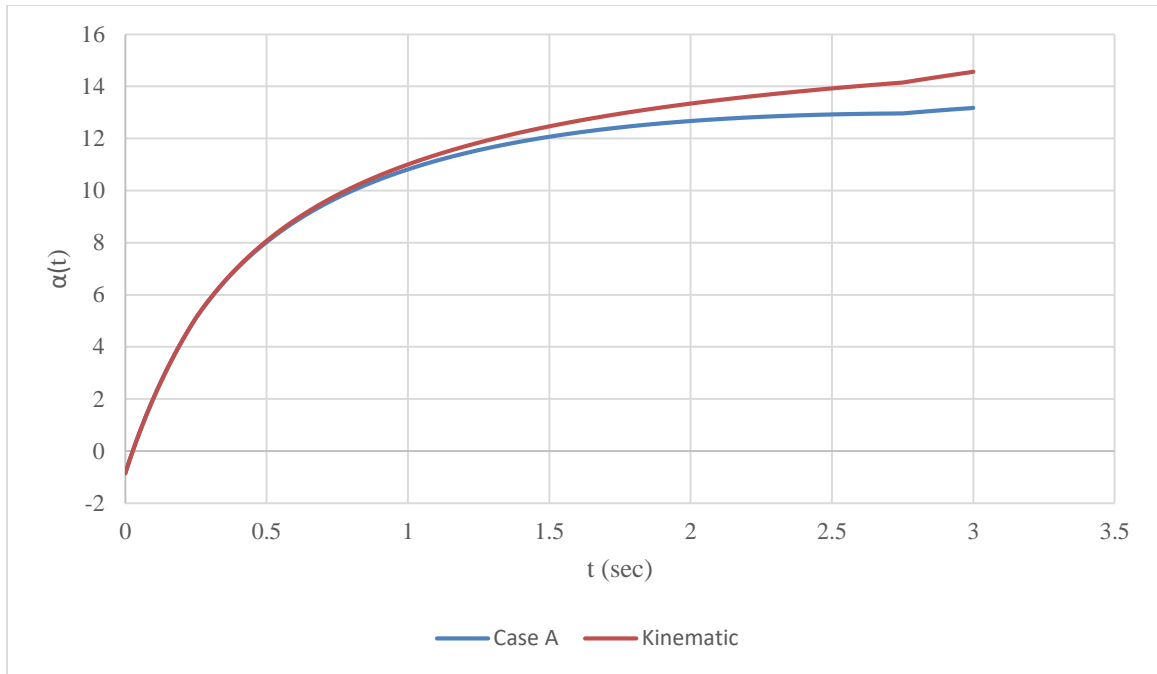
Figure 33: Case A Trajectory x(t) Compared to Kinematic Solution

SECTION III: COMPARISION TO PREVIOUS LAUNCH

In a previous study, a lighter-weight mass simulator was launched with a similar, but different configuration, namely one with the rocket thrust vector at a 7° angle to the longitudinal axis of the mass simulator, which was down to impart a pitch up moment, with pitch up being more favorable than pitch down. Video of the test launch was analyzed using Tracker Video Analysis and Modeling Tool as shown in Figure 36 and a comparison of the results is made from those of this study in Table 4 below. This software takes raw video, and the user specifies the datum and center of mass in each frame, the software uses this input to generate a plot of the object trajectory.

Figure 34: Video Analysis of Previous Launch using Tracker Software

Table 4: Comparison to Video Analysis

This Study	Video Analysis
$V_{t=1.93}= 250$ ft/s	$V_{t=1.929}= 352$ ft/s
$x_{t=1.93}= 288.7$ ft	$x_{t=1.929}= 291.6$ ft
$z_{t=1.93}= 54.1$ ft	$z_{t=1.929}= 221.9$ ft

The differences in velocity and vertical displacement are likely due primarily to the introduction of an angle between the RATO bracket and the mass simulator in the previous system. This would direct more of the rocket thrust force in the vertical direction, causing a higher flight path to be reached. Additionally, the video analyzed was rather shaky, this noise in the data is shown in Figure 34 above.

SECTION IV: SENSATIVITY STUDY

Considering the variance in lift and drag coefficient results given by the mesh geometry used in the alpha sweep compared to finer meshes, as well as the variations shown with the 2D mesh verification, a sensitivity study was performed to verify the usage of these values. Here the coefficients of lift and drag were altered by +/- 20%, as shown below, the coefficient of lift was decreased by 20%, while a 20% increase in the coefficient of drag was used to give a worst-case

scenario. As can be seen, the differences in the state histories of the mass simulator during launch are nearly imperceptible, especially compared to the differences generated by slight changes of the rocket motor alignment relative to the longitudinal axis of the mass simulator as shown in Figures 35-39 additionally, these figures show a comparison of a 5% increase in thrust output at all intervals, which again, has a significantly greater effect on the state histories than changes in the drag polar values. Lastly, the results from kinematic analysis are also given.
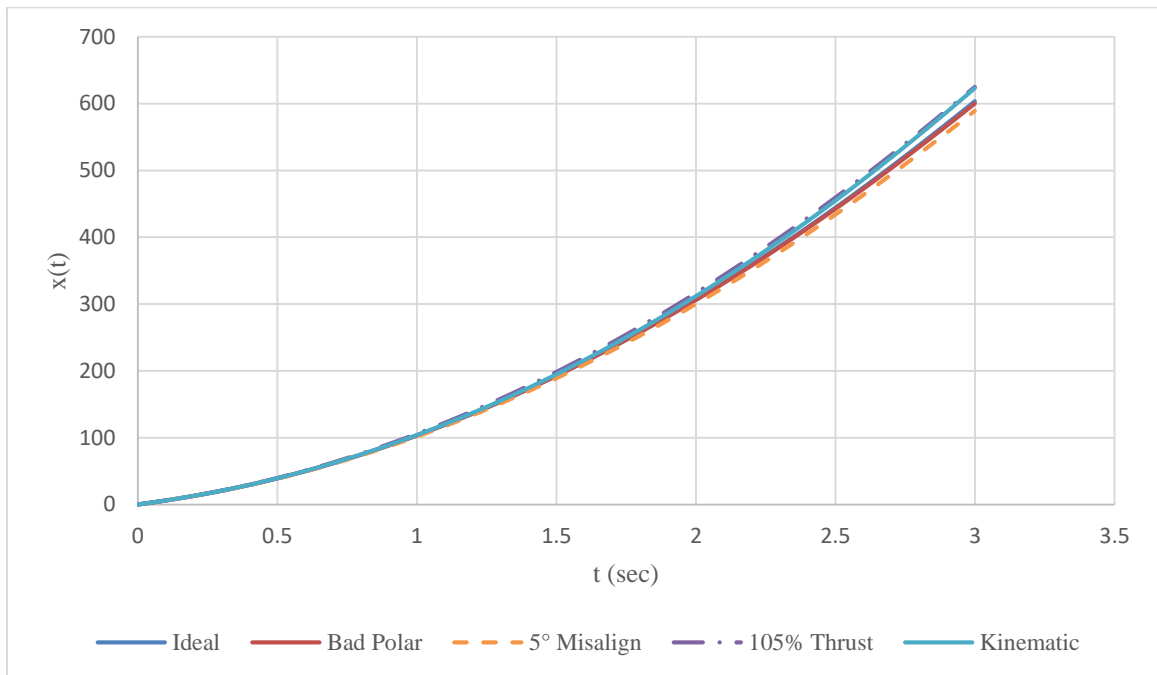
Figure 35: Comparison of x(t)
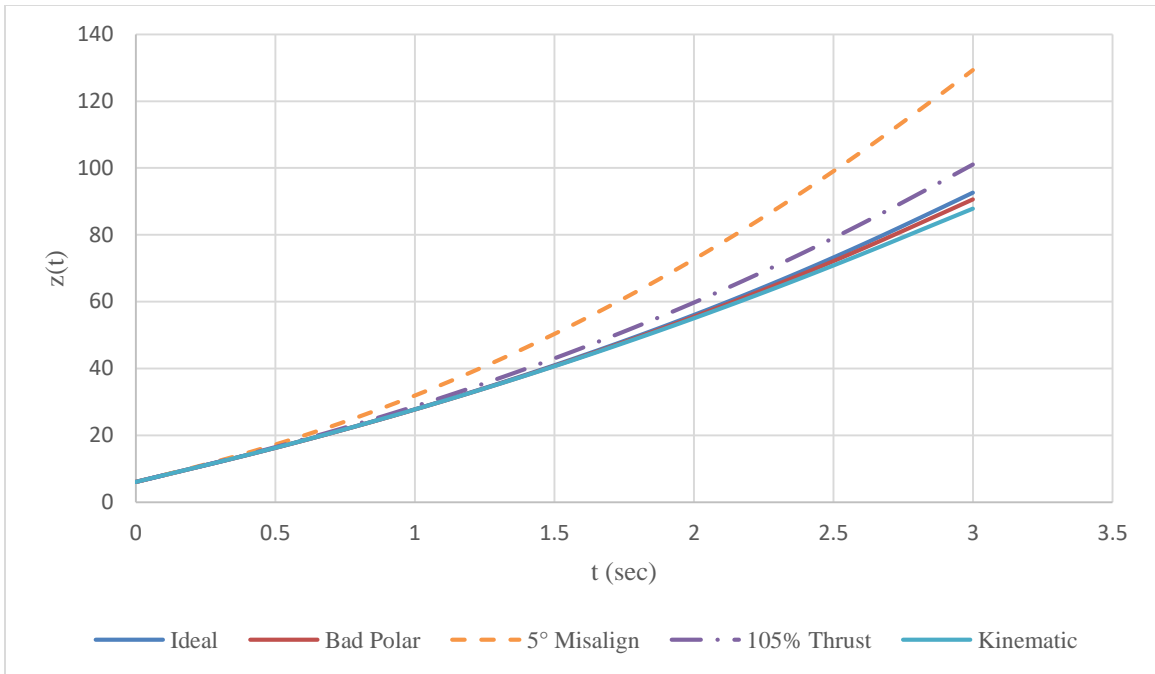
Figure 36: Comparison of z(t)
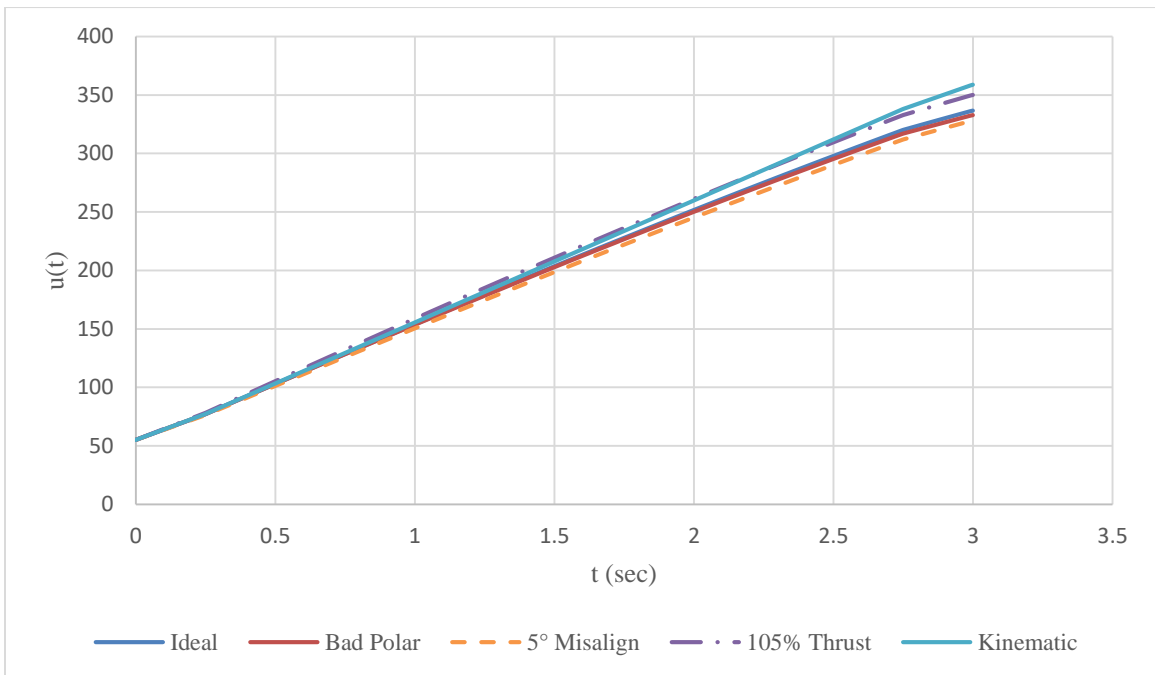
Figure 37: Comparison of u(t)
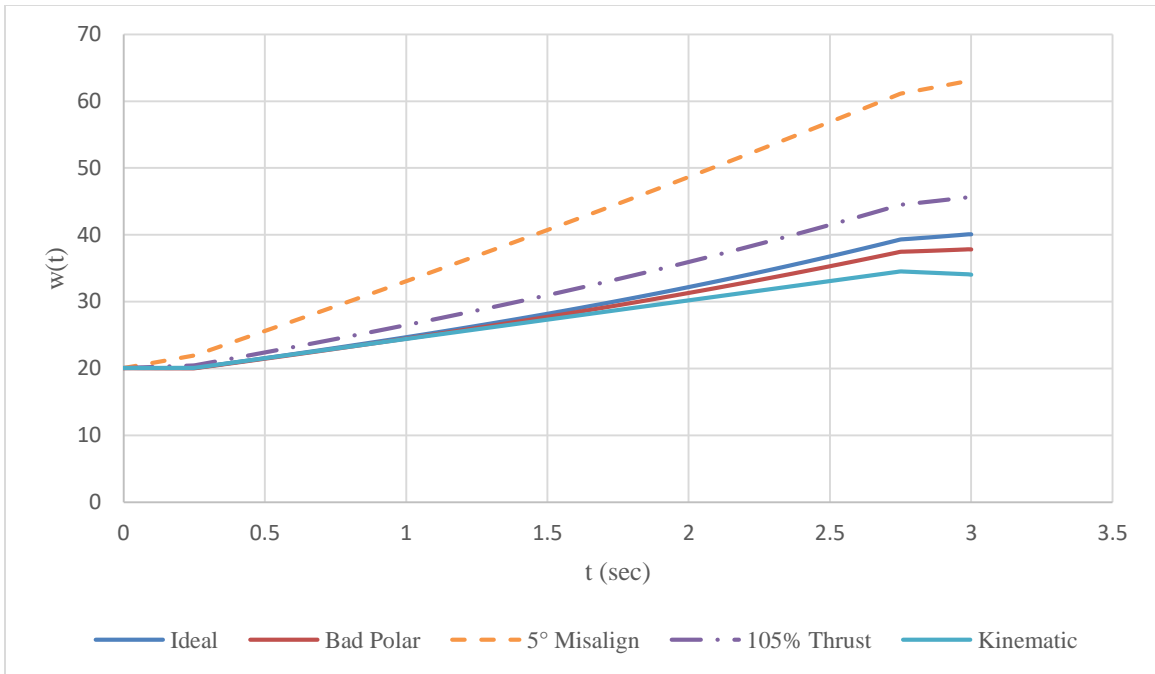
Figure 38: Comparison of w(t)
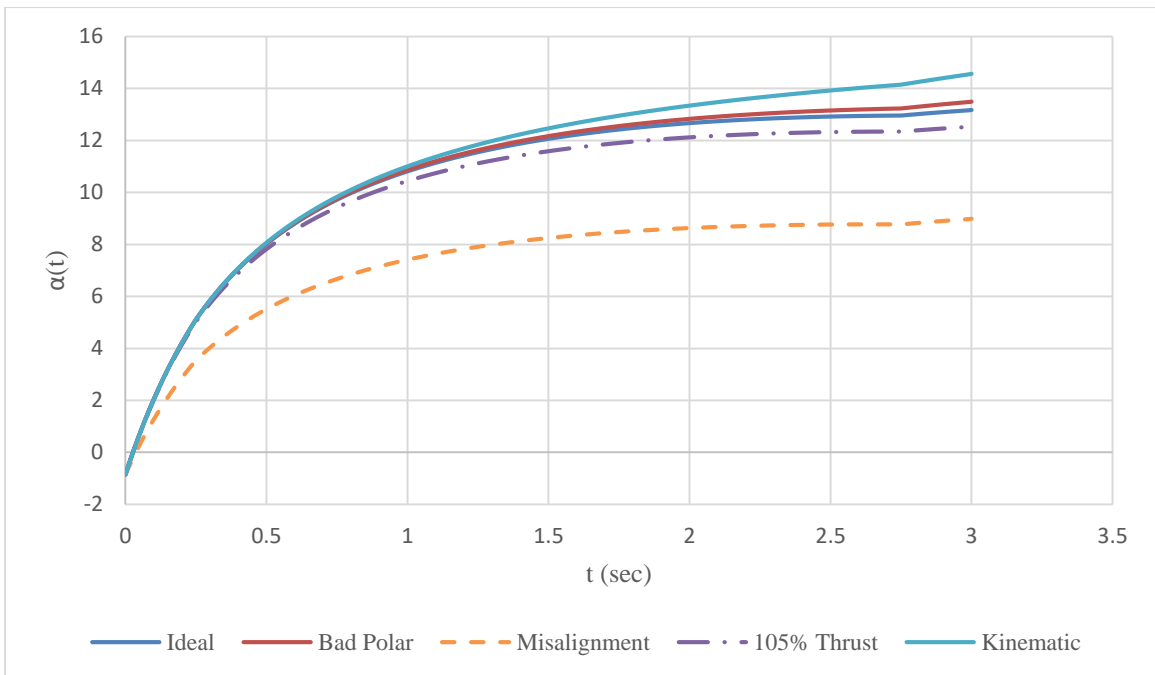
Figure 39: Comparison of α(t)

37

Given the relative insensitivity of the state history results to variations in the aerodynamic characteristics of the mass simulator, it is concluded that these results are sufficiently accurate to estimate the effects of aerodynamic forces on the trajectory and attitude of the mass simulator during these first three seconds of flight after launch. This result indicates that the CFD parameters given in Case A in Chapter III were sufficient for the scope of this study and that further grid refinement is not a current priority. It is important to note that areas that significantly impacted the CFD results included mesh density near the mass simulator, which could be refined in later studies. However, more impactful factors include RATO bracket alignment and rocket motor thrust variances, of which, further analysis should take priority over grid refinement. These principles of analysis can be applied to future analysis of mass simulators, given a similar configuration, for use in testing rocket-assisted take-off systems and motors for unmanned aircraft.

CHAPTER V

CONCLUSION

Based on the state histories generated by the launch simulator, the trajectory and attitude of the

mass simulator appears favorable during the first three seconds of flight after launch. After this

period of flight, high enough air speeds will be reached for the control surfaces of high-speed

unmanned aircraft benefitting from rocket-assisted take-off to be effective in controlling said

aircraft and maintaining stable flight. However, further investigation must be done to account for

variables induced during manufacturing, such as bracket and motor alignment tolerances, in

addition to analysis of rocket motor thrust variance effects through further sensitivity studies and

analysis. Once other factors impacting the longitudinal static stability of the mass simulator

during launch are isolated and modeled, a higher fidelity computational fluid dynamics model of

the system could be pursued.

Recommendations to refine the computational fluid dynamics model include turbulent boundary

layer simulation rather than modeling, which could be achieved by further refining the prism

layer geometry, with one method to consider being the use of adaptive prism layer refinement.

Additionally, other meshers could be utilized to increase the effectiveness of the adaptive mesh

refinement. Along with refining the aerodynamic model of the mass simulator, refinement of the

launch simulator would allow more parameters to be explored.

Parameters that would improve the applicability of the launch simulator include accounting for pitch moment, inertial characteristics, and asymmetric thrust profiles of the rocket motors, which could be used to account for variability in rocket motor ignition and performance.

Overall, this study has determined that the aerodynamic characteristics alone of this mass simulator, in conjunction with the rocket-assisted take-off system are suitable for launch in regard to longitudinal stability.

Lastly, this study has concluded that the framework laid out within provides sufficient analysis of the aerodynamic forces on this system to determine the practical effects they have on the longitudinal static stability during launch. Recommendations for future studies include the simplification of complex geometries such as sharp edges, protruding fasteners, threads, and fittings. For more streamlined bodies with lifting surfaces and aerodynamic coefficients that may be more sensitive to these small features, modeling these features may have significant impact on the results of the computational fluid dynamics model and should still be considered. However, in the case of mass simulators such as the one presented in this study, simplifying these features would significantly reduce the computational model complexity and therefore computational demand, allowing quicker model refinement, while having minimal impact on the gross aerodynamic model of the system.

REFERENCES

[1]   J. Gundlach, Designing Unmanned Aircraft Systems: A Comprehensive Approach, American Institute of Aeronautics and Astronautics, 2014.

[2]   R. Austin, Unmanned Aircraft Systems: UAV's Design, Development and Deployment, American Institute of Aeronautics and Astronautics, 2010.

[3]   W. Yang, Y. Wang, P. Zhang and Y. Liu, "Potential Development of Linear Motors for," IEEE TRANSACTIONS ON APPLIED SUPERCONDUCTIVITY, vol. 20, no. 3, 2010.

[4]   B. Reck, "First Design Study of an Electrical Catapult for Unmanned Air Vehicles in the Several Hundred Kilogram Range," IEEE TRANSACTIONS ON MAGNETICS, vol. 39, no. 1, 2003.

[5]   M. M. Hussain, B. A. Siddiqui and A. Memon, "Design And Analysis Of Rocket Assisted Take-off High-Speed UAV," in IEEE 6th International Conference on Aerospace Science and Engineering, Islamabad, 2019.

[6]   R. W. Beard and T. W. McLain, Small Unmanned Aircraft: Theory and Practice, Princeton: Princeton University Press, 2012.

[7]   M. M. Sarigul-Klijn, N. Sarigul-Klijn, G. Hudson and C. Brown, "A New Air Launch Concept: Vertical Air Launch Sled (VALS)," in AIAA SPACE 2012 Conference & Exposition, Pasadena, 2012.

[8]   A. R. Collazo Garcia III, P. Ranjan, K. J. Chen, K. A. James and P. J. Ansell, "Flight Trajectory Optimization of Sailplane After Rope Break," Journal of Aircraft, vol. 58, no. 6, pp. 1229-1241, 2021.

[9]   J. Francis, "Launch system for unmanned aerial vehicles for use on ran patrol boats," in The UNSW Canberra at ADFA Journal of Undergraduate Engineering Research, Canberra , 2011.

[10]   R. Davis, "The Design and Development of a Fixed Wing UAS for use on RAN Patrol Boats," in The UNSW Canberra at ADFA Journal of Undergraduate Engineering Research, Canberra, 2009.

[11]   M. C. Stracker, An Operational Manpower Analysis Of The RQ-8 Fire Scout Vertical Take-Off Unmanned Aerial Vehicle (VTUAV), Montery, California: Naval Postgraduate School, 2007.

[12]   J. D. Anderson, K. R. Bruggemeyer, C. J. Rathman and M. D. Sallaz, Soerbitol Motor Casting and Performance, Stillwater: Oklahoma State University, 2021.

[13]   D. Velasco, G. Copher, R. Ize, J. Bertels, K. P. Rouser and C. D. Totty, Design, Manufacturing, and Test of Low-Cost Small Composite Solid Rocket Motors, Stillwater: Oklahoma State University, 2021.

[14]   K. J. Moody, A. M. Walsh, A. D. Ngo, S. Whyte, A. Stottlemyre and K. P. Rouser, "Development of Sorbitol-Based Solid Rocket Motors for Propulsion Education," in AIAA Scitech 2020 Forum, Orlando, 2020.

[15]   P. G. Fahlstrom and T. J. Gleason, Introduction to UAV Systems, 4th Edition, Hoboken: John Wiley & Sons, Ltd, 2012.

[16]   J. D. Mattingly, K. M. Boyer and H. von Ohain, Elements of propulsion: gas turbines and rockets, Reston, VA: American Institute of Aeronautics and Astronautics, 2006.

[17]   V. Yemets, P. Harkness, M. Dron', A. Pashkov, K. Worrall and M. Middleton, "Autophage Engines: Toward a Throttleable Solid Motor," Journal of Spacecraft and Rockets, vol. 55, no. 4, pp. 984-992, 2018.

[18]   S. D. Heister, W. E. Anderson, T. L. Pourpoint and R. J. Cassady, Rocket Propulsion, Cambridge: Cambridge University Press, 2019.

[19]   R. C. Hibbeler, Engineering Mechanics: Statics and Dynamics, Hoboken: Pearson Prentice Hall, 2016.

[20]   C. D. Perkins, "Development of Airplane Stability and Control Technology," Journal of Aircraft, vol. 7, no. 4, pp. 290-301, 1970.

[21]   T. M. Foster, Dynamic Stability and Handling Qualities of Small Unmanned Aerial-Vehicles, Provo: Bringham Young University, 2005.

[22]   D. Raymer, Aircraft Design: A Conceptual Approach, Reston: American Institute of Aeronautics and Astronautics, 2012.

[23]   J. Anderson, Fundamentals of Aerodynamics, New York: McGraw-Hill Education, 2017.

[24]   R. C. Nelson, Flight Stability and Automatic Control, New York: The McGraw-Hill Companies, 1998.

[25]   S. A. Brandt, Introduction to Aeronautics: A Design Perspective, Reston, VA: American Institue of Aeronautics and Astronautics, 2004.

[26]   B. Etkin and L. D. Reid, Dynamics of Flight: Stability and Control, New York: John Wiley & Sons, Inc., 1996.

[27]   F. Saltara, A. D'Agostini Neto and J. Lopez, "3D CFD Simulation of Vortex-induced Vibration of Cylinder," International Journal of Offshore and Polar Engineering, vol. 21, no. 3, 2011.

[28] J. Anderson, Computational Fluid Dynamics: The Basics with Applications, Singapore: McGraw-Hill Book Co., 1995.

[29] D. Rohlf, S. Schmidt and J. Irving, "Stability and Control Analysis for an Unmanned Aircraft," Journal of Aircraft, vol. 49, no. 6, pp. 1597-1609, 2012.

[30] K. W. Iliff, "Parameter estimation for flight vehicles," Journal of Guidance, Control, and Dynamics, vol. 12, no. 5, pp. 609-622, 1989.

[31] A. Rizzi, "Modeling and simulating aircraft stability and control—The SimSAC project," Progress in Aerospace Sciences, vol. 47, no. 8, pp. 573-588, 2011.

[32] M. Ghoreyshi, D. Vallespin, A. Da Ronch, K. Badcock, J. Vos and S. Hitzel, "Simulation of Aircraft Manoeuvres based on Computational Fluid Dynamics," in AIAA Atmospheric Flight Mechanics Conference, Toronto, 2012.

[33] M. Allan, K. Badcock and B. Richards, "CFD Based Simulation of Longitudinal Flight Mechanics with Control," in 43rd AIAA Serospace Sciences Meeting & Exhibit, Reno, 2012.

[34] Y. Zou, X. Zhao and Q. Chen, "Comparison of STAR-CCM+ and ANSYS Fluent for simulating indoor airflows," Building Simulation, pp. 165-174, 2018.

[35] E. Saiki and S. Biringen, "Numerical Simulation of a Cylinder in Uniform Flow: Application of a Virtual Boundary Method," Journal of Computational Physics, vol. 123, no. 2, pp. 450-465, 1996.

[36] L. Baranyi and R. I. Lewis, "Comparison of a grid-based CFD method and vortex dynamics predictions of low Reynolds number cylinder flows," The Aeronautical Journal, vol. 110, no. 1103, pp. 63-71, 2016.

[37] J. F. Wendt, Computational Fluid Dynamics: An Introduction, New York: Springer, Berlin, Heidelberg, 2009.

[38] A. Cleaver, "Rockets and Assisted Take-Off," The Journal of the Royal Aeronautical Society, vol. 55, no. 482, pp. 87-109, 1951.

[39] H. Y. Irwanto, "Rocket booster effect on RKX-200TJ flight stability," in 2015 4th International Conference on Instrumentation, Communications, Information Technology, and Biomedical Engineering (ICICI-BME), Bandung, 2015.

[40] H. Irwanto, "HILS of auto take off system: For high Speed UAV using booster rocket," in 2016 International Seminar on Intelligent Technology and Its Applications (ISITIA), Mataram, 2016.

[41] C. Rathman, S. Robbins, S. Francis and J. Mobley, A Mass Simulator for Development of Rocket-Assisted Take-Off Systems for Unmanned Aircraft, Stillwater: Oklahoma State University, 2021.

[42] T. A. Eymann and J. D. Martel, "Numerical Investigation of Launch Dynamics for Subscale Aerial Drone with Rocket Assisted Take-Off (RATO)," in U.S. Air Force T&E Days, Los Angeles, 2008.

[43]   J. D. Martel and J. G. Dudley, "External Pitching Moment (EPM) due to Turbine Engine Exhaust Impingement on Rocket Assisted Take Off (RATO) Bottle," in 45th AIAA Aerospace Sciences Meeting and Exhibit, Reno, 2007.

[44]   R. L. Panton, Incompresible Flow, Hoboken: John Wiley & Sons, Inc., 2013.

APPENDICES

APPENDIX A: CFD Results for ALPHA SWEEP of Case A
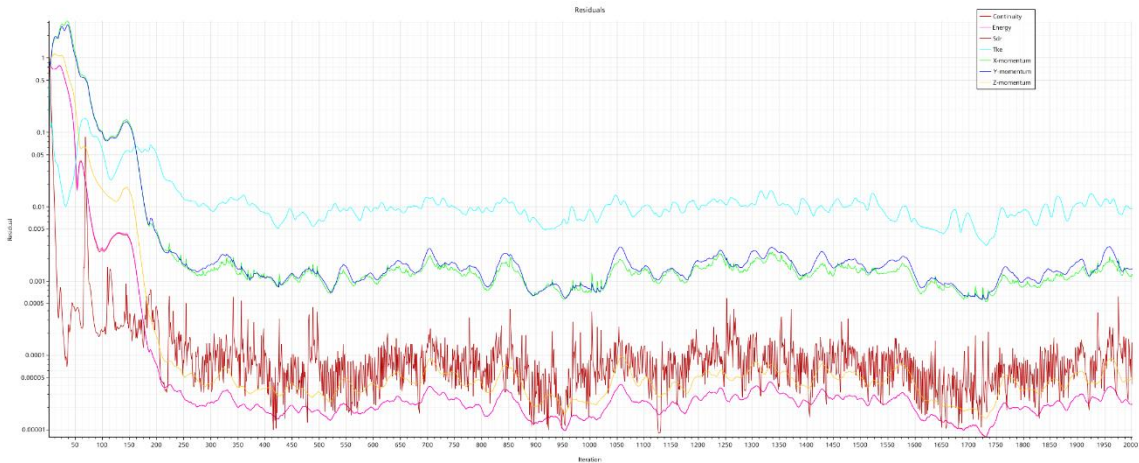
Figure 40: Residuals at α= -15°
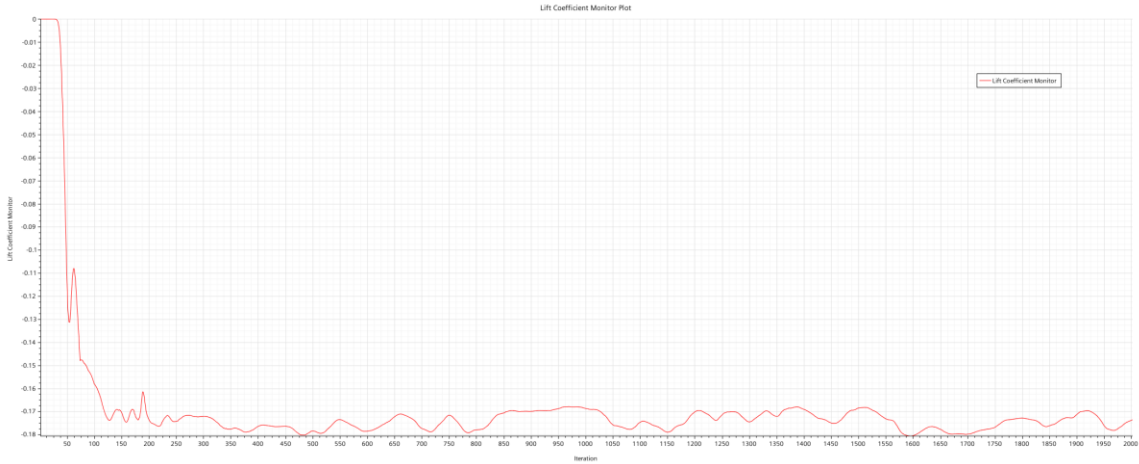
Figure 41: :Lift Coefficient at α= -15°
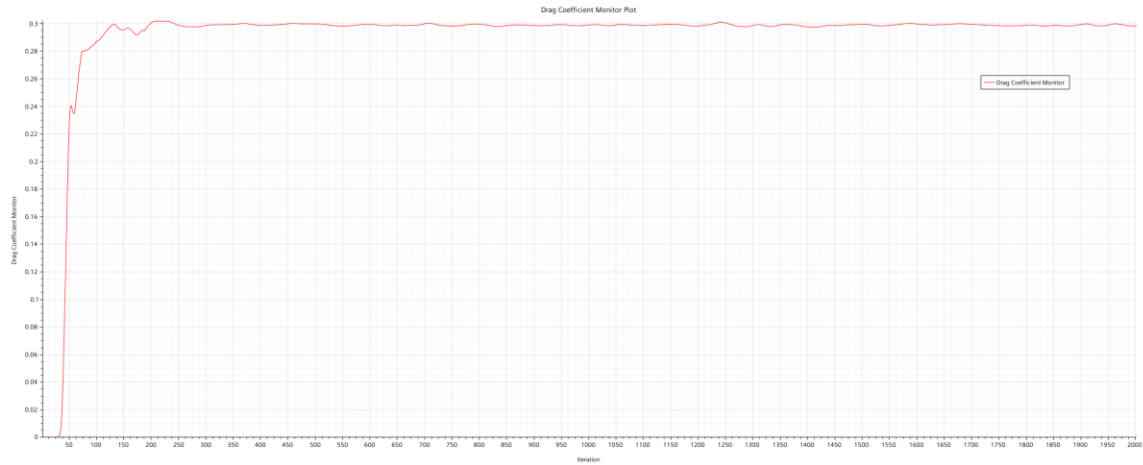
Figure 42: Drag Coefficient α= -15°
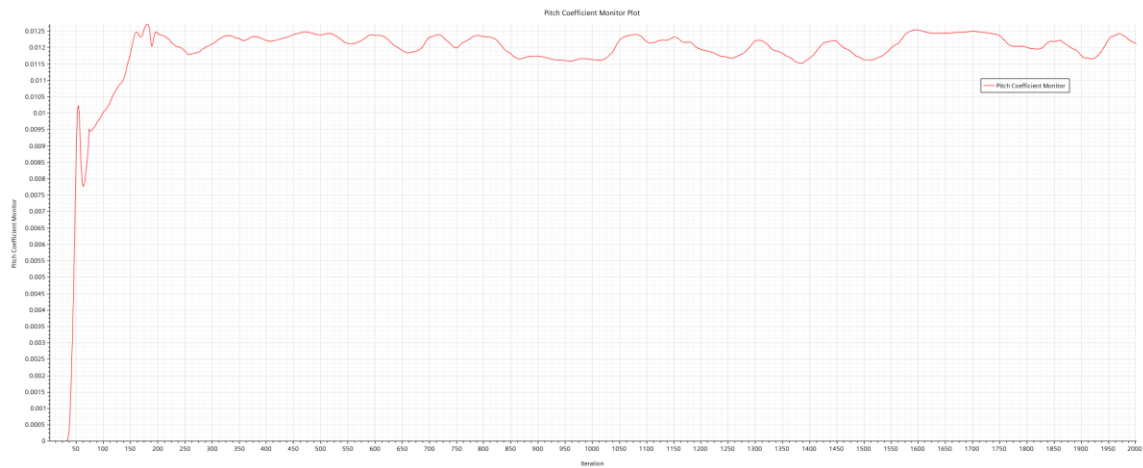
Figure 43: Pitch Moment Coefficient α= -15°
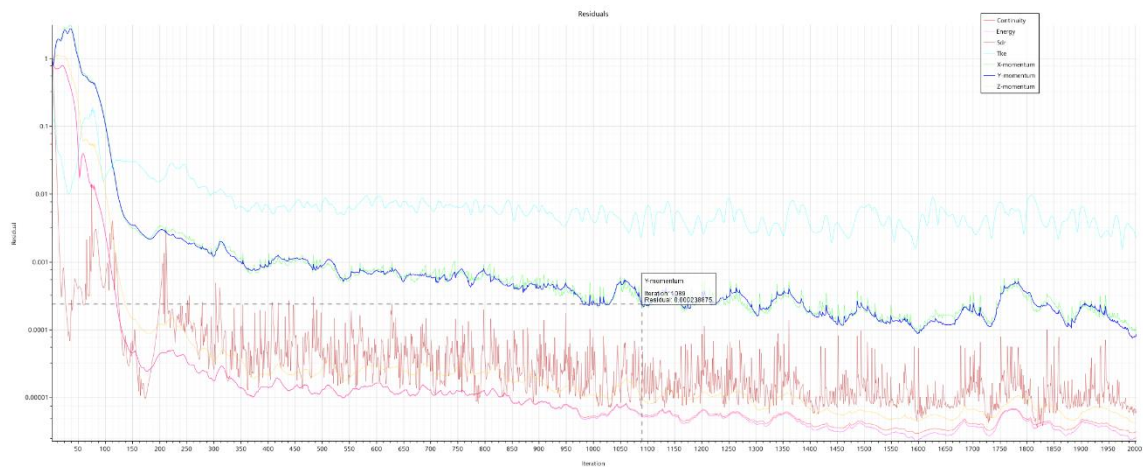
Figure 44: Residuals α= -12.5°

46
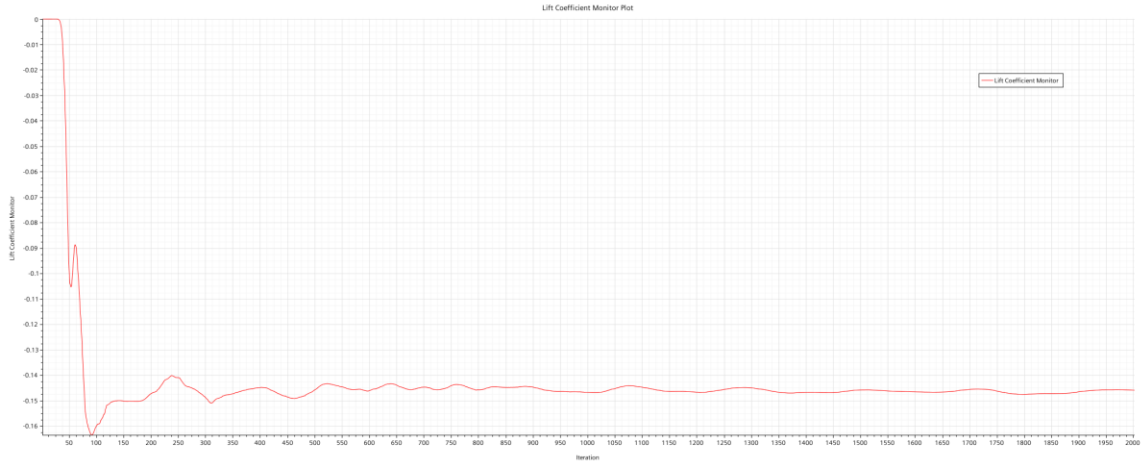
Figure 45: Lift Coefficient at α= -12.5°
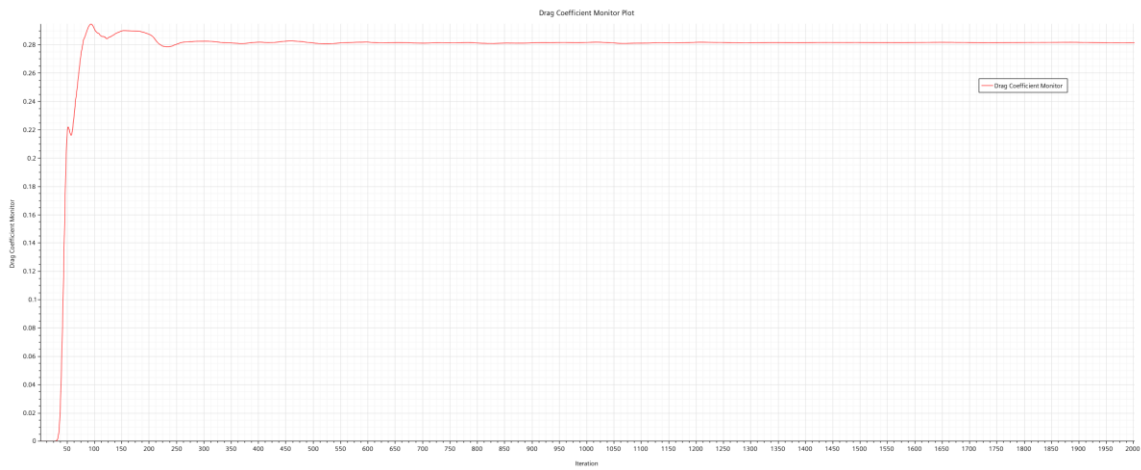
Figure 46: Drag Coefficient at α= -12.5°
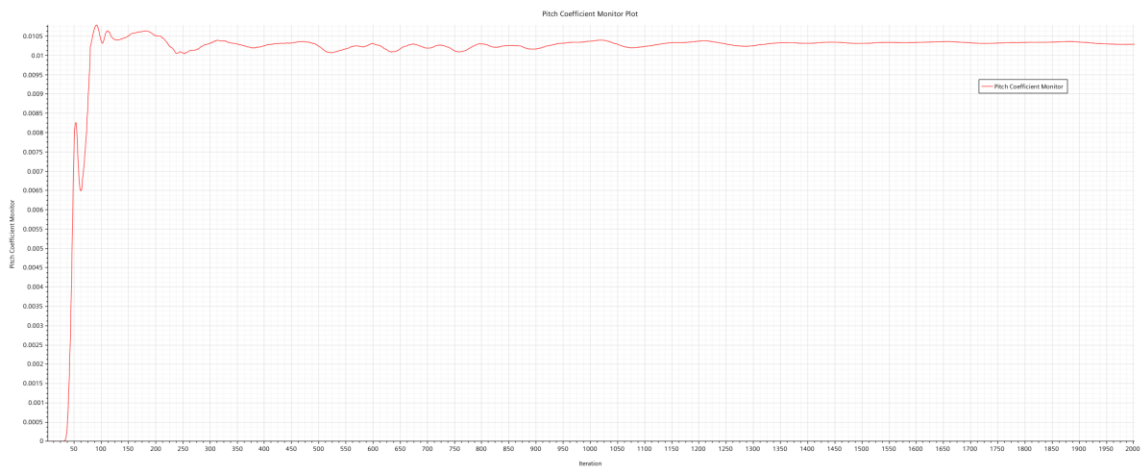
Figure 47: Pitch Moment Coefficient at α= -12.5°

Figure 48: Residuals at α= -10°
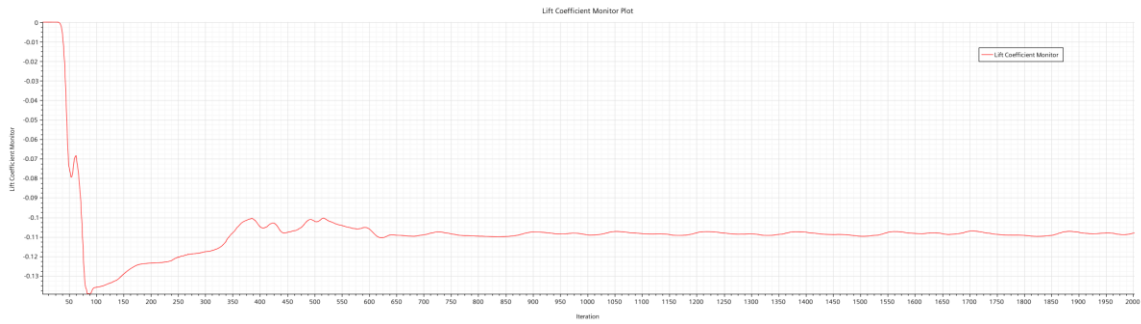
Figure 49: Lift Coefficient at α= -10°
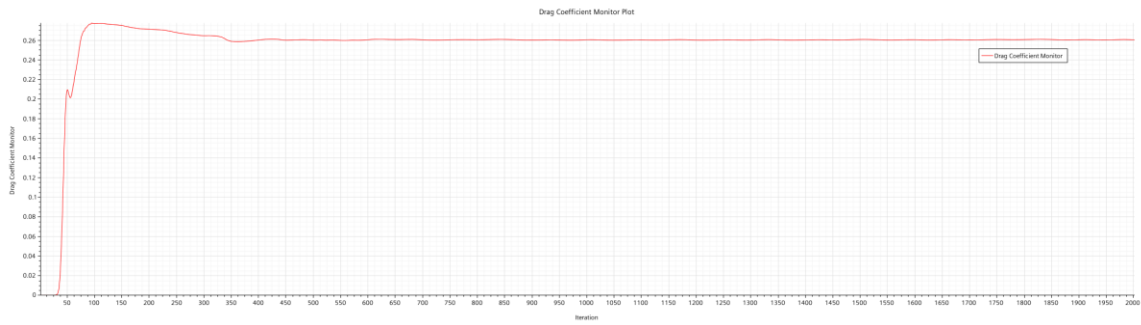
Figure 50: Drag Coefficient at α= -10°
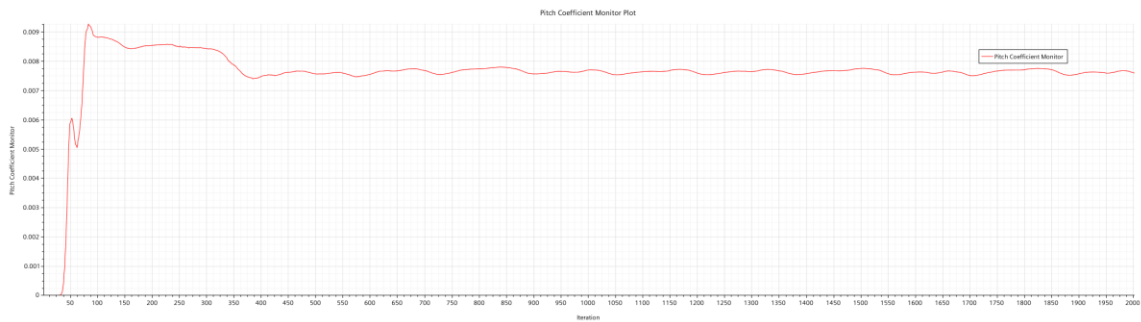
Figure 51: Pitch Moment Coefficient at α= -10°

Figure 52: Residuals at α= -7.5°
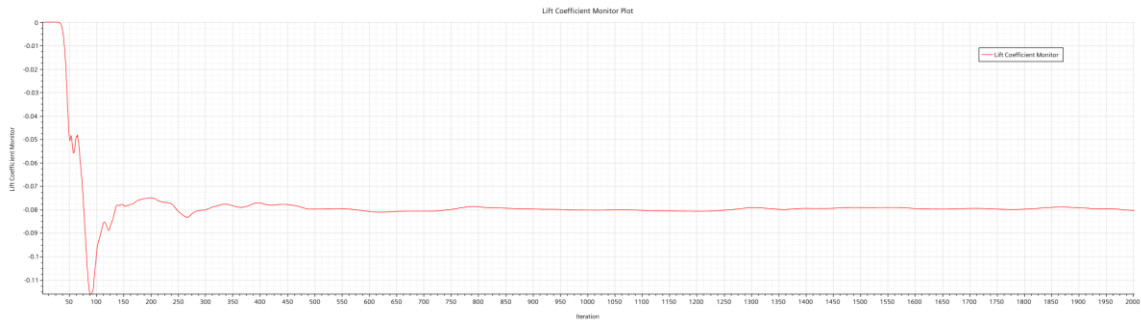
Figure 53: Lift Coefficient at α= -7.5°
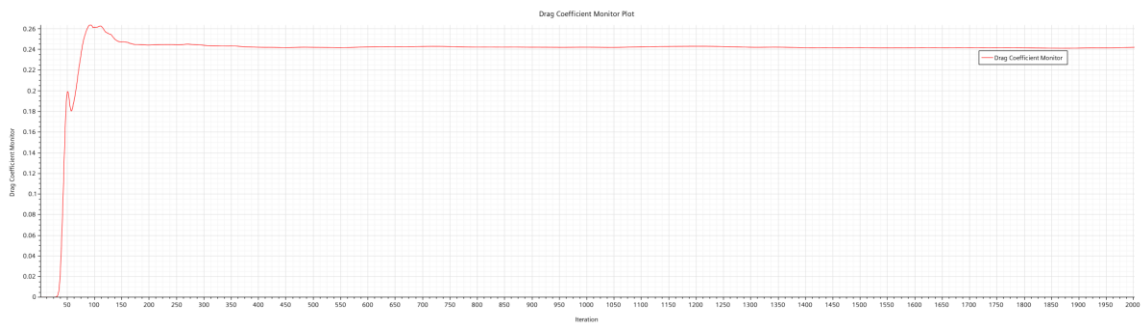
Figure 54: Drag Coefficient at α= -7.5°
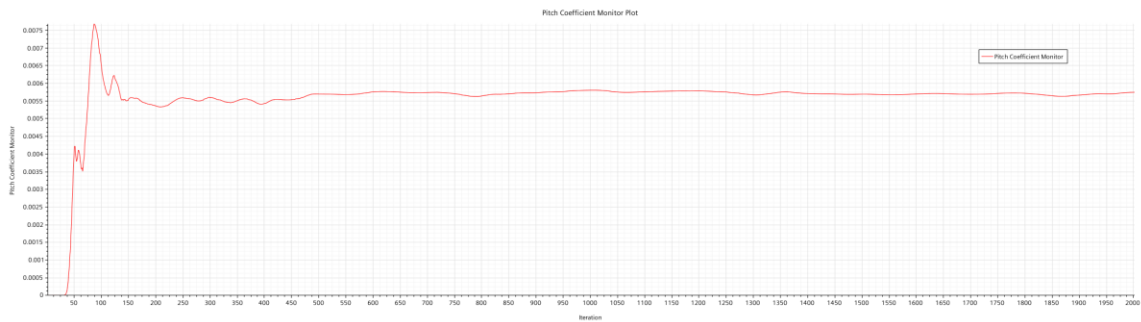
Figure 55: Pitch Moment Coefficient at α= -7.5°

49
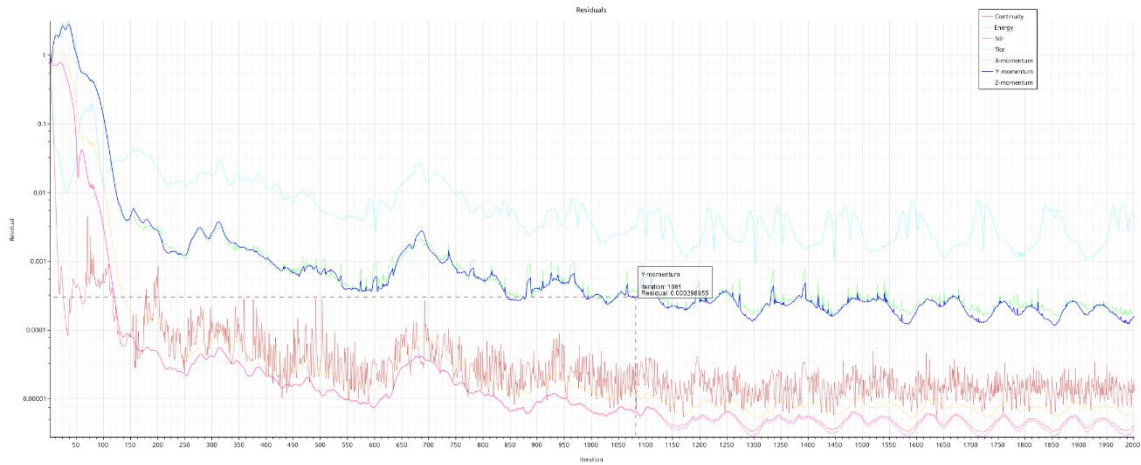
Figure 56: Residuals at α= -5°
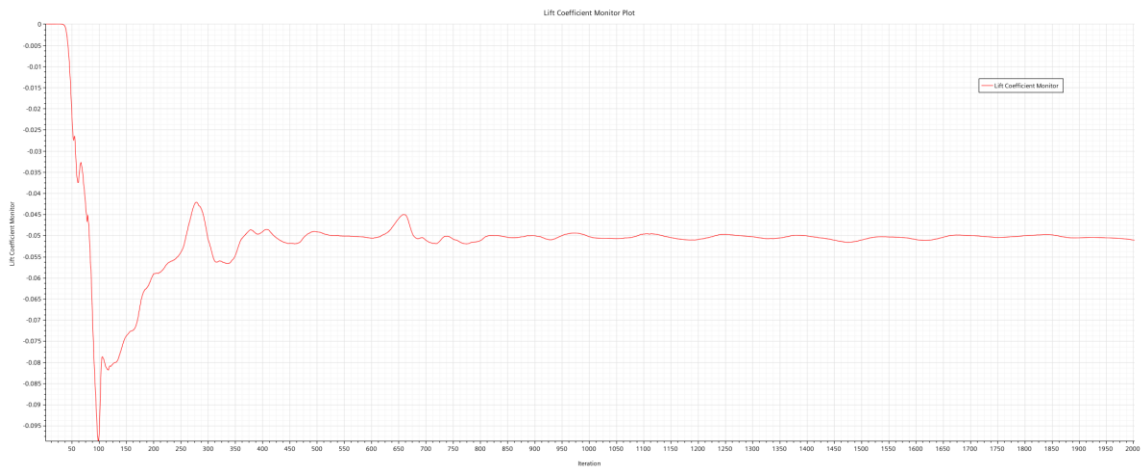
Figure 57: Lift Coefficient at α= -5°
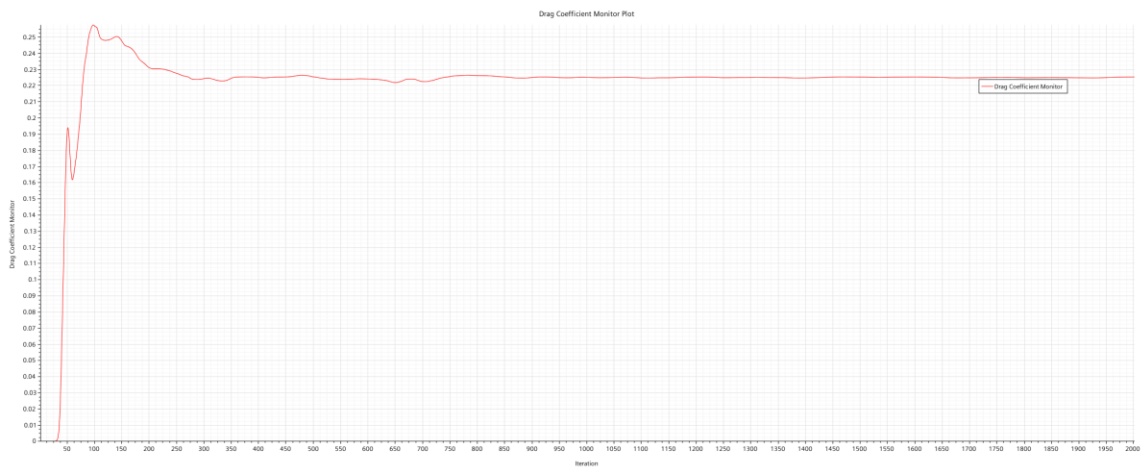
Figure 58: Drag Coefficient at α= -5°

50
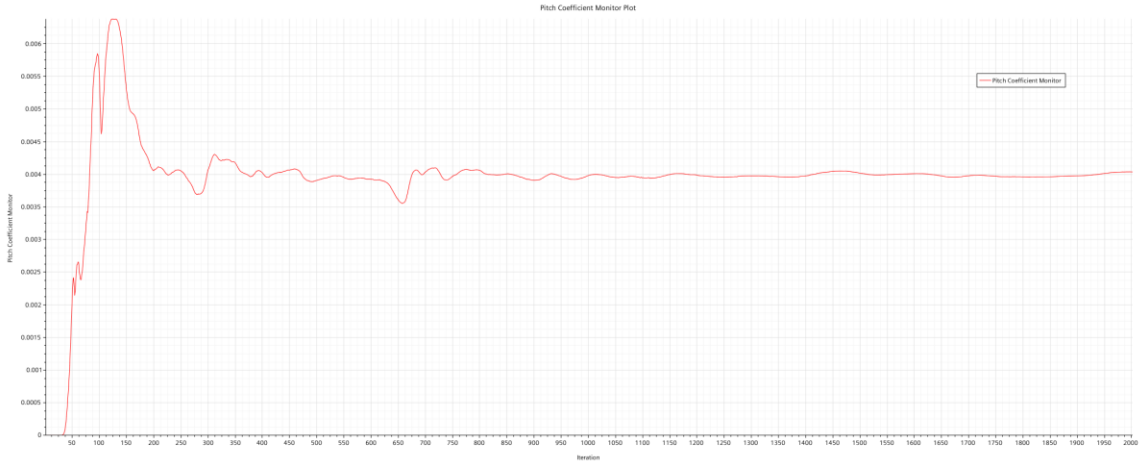
Figure 59: Pitch Moment Coefficient at α= -5°
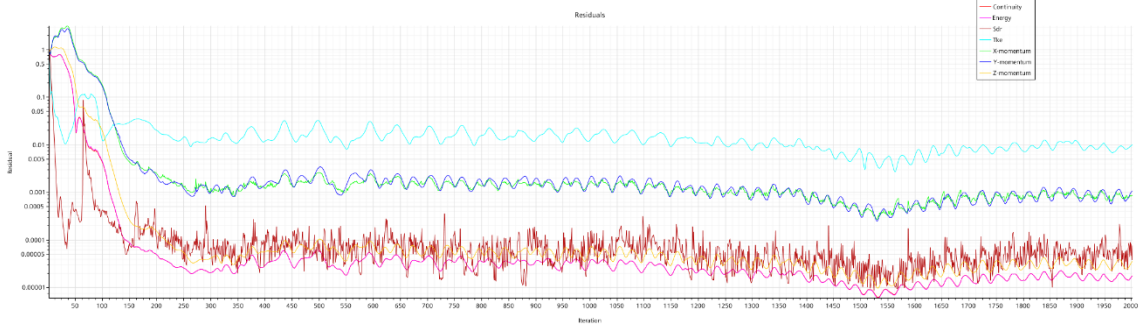
Figure 60: Residuals at α= -2.5°
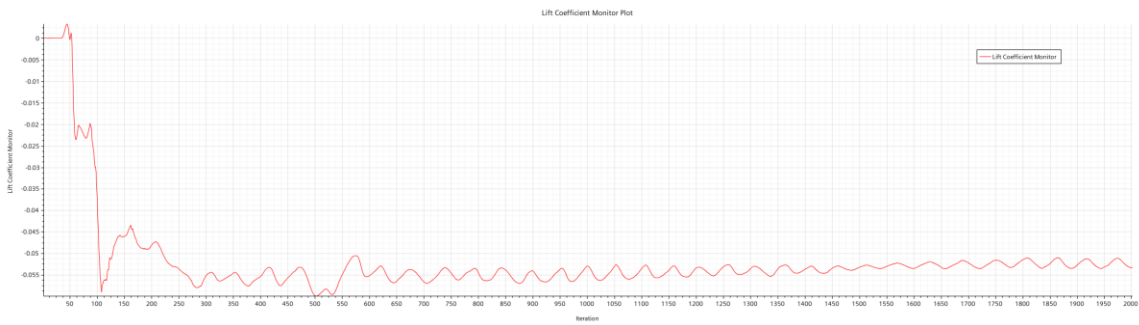
Figure 61: Lift Coefficient at α= -2.5°
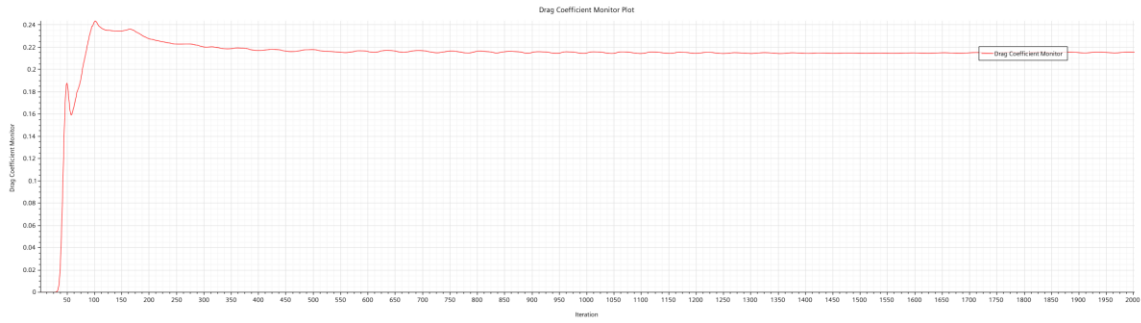
Figure 62: Drag Coefficient at α= -2.5°
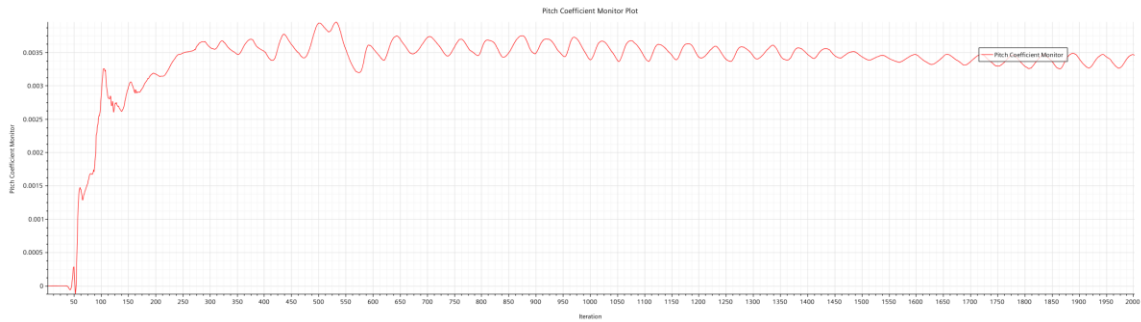
Figure 63: Pitch Moment Coefficient at α= -2.5°
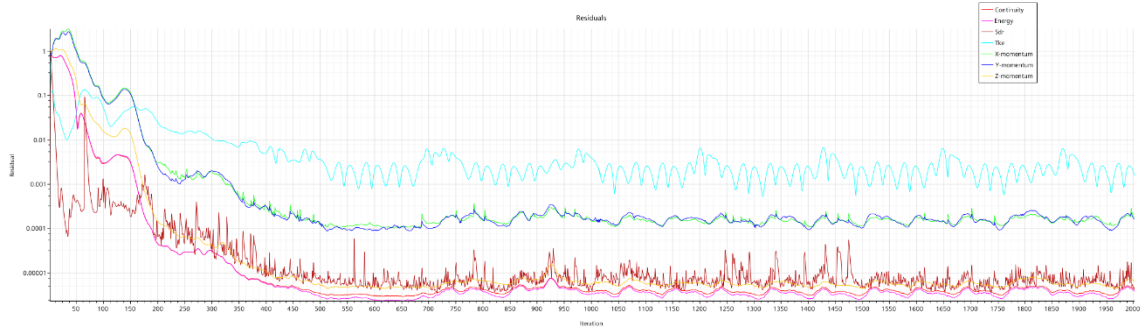
Figure 64: Residuals at α= 0°
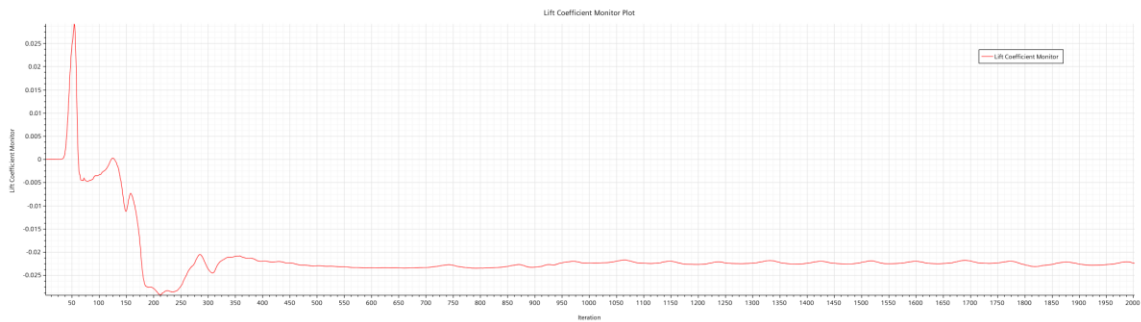
Figure 65: Lift Coefficient at α= 0°
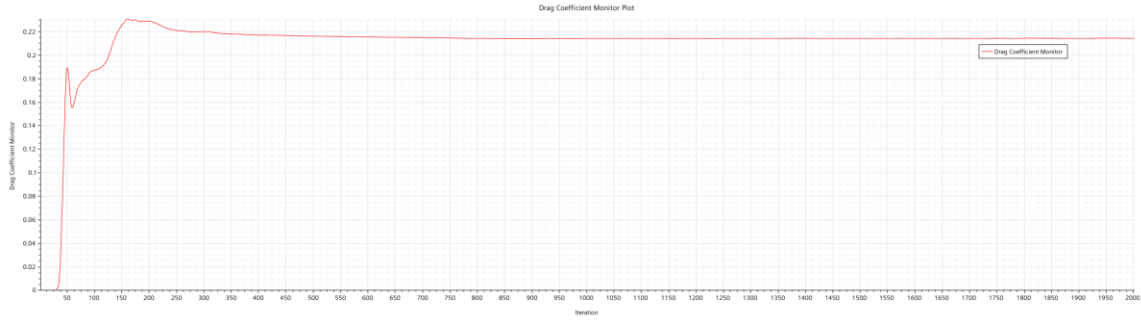
Figure 66: Drag Coefficient at α= 0°
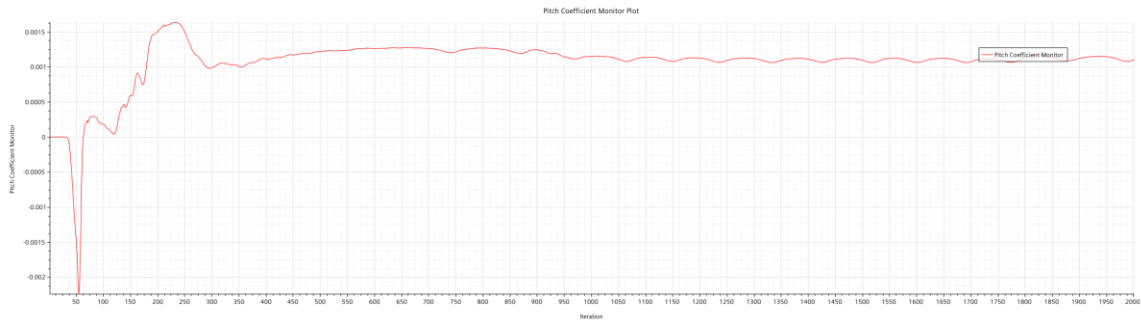
Figure 67: Pitch Moment Coefficient at α= 0°
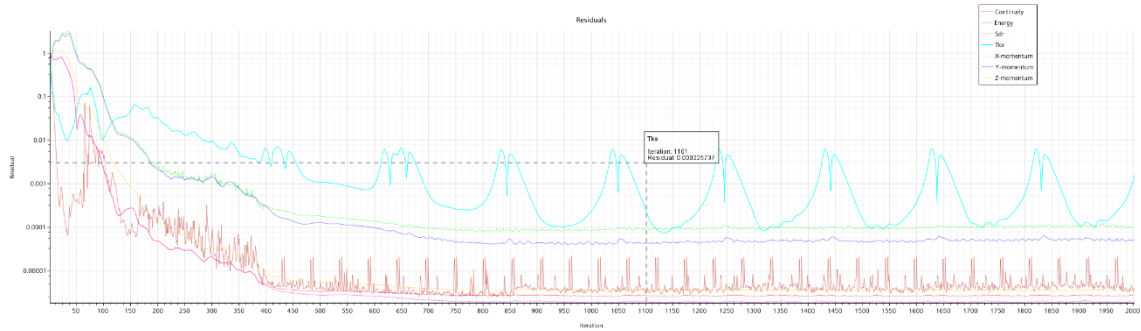
Figure 68: Residuals at α= 2.5°
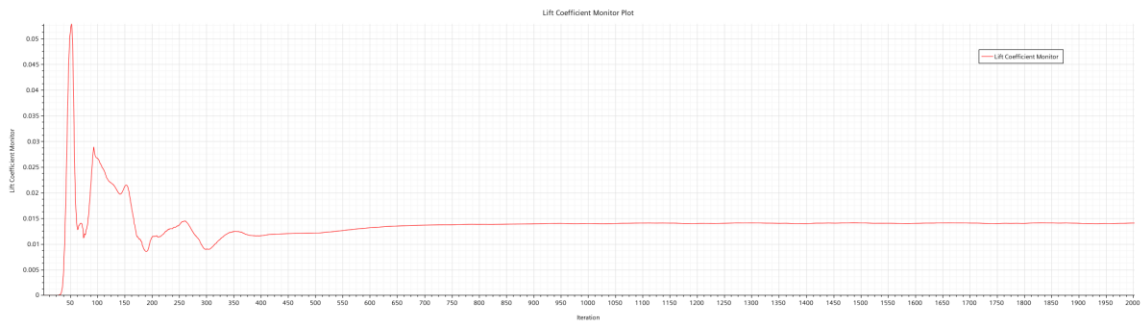
Figure 69: Lift Coefficient at α= 2.5°
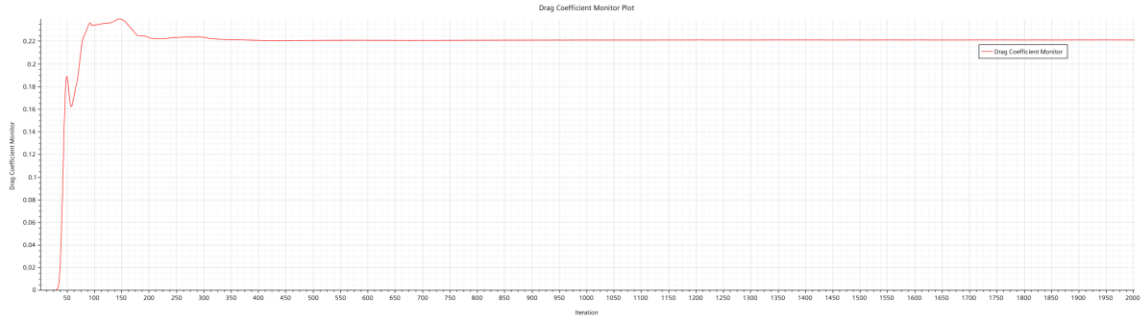
Figure 70: Drag Coefficient at α= 2.5°
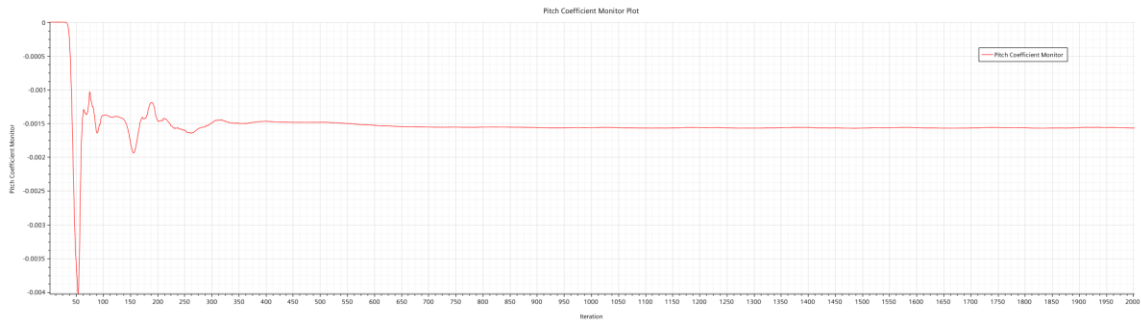
Figure 71: Pitch Moment Coefficient at α= 2.5°
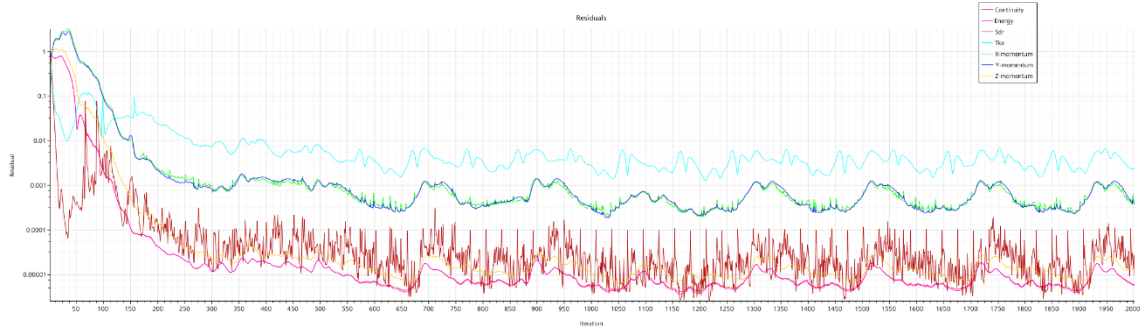
Figure 72: Residuals at α= 5°
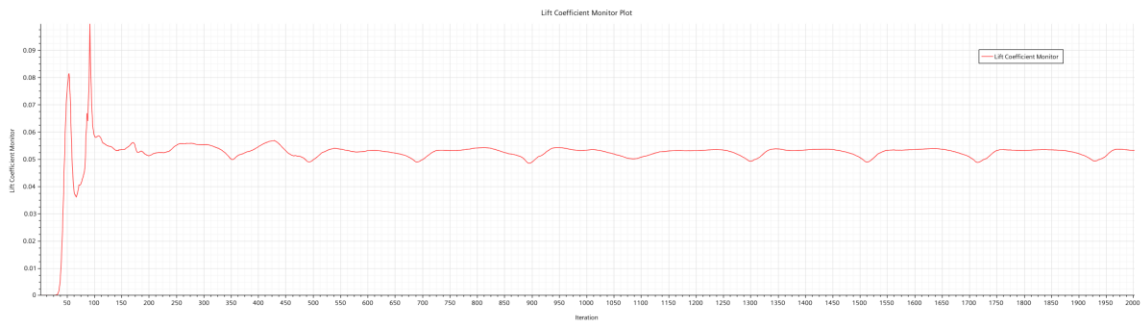
Figure 73: Lift Coefficient at α= 5°
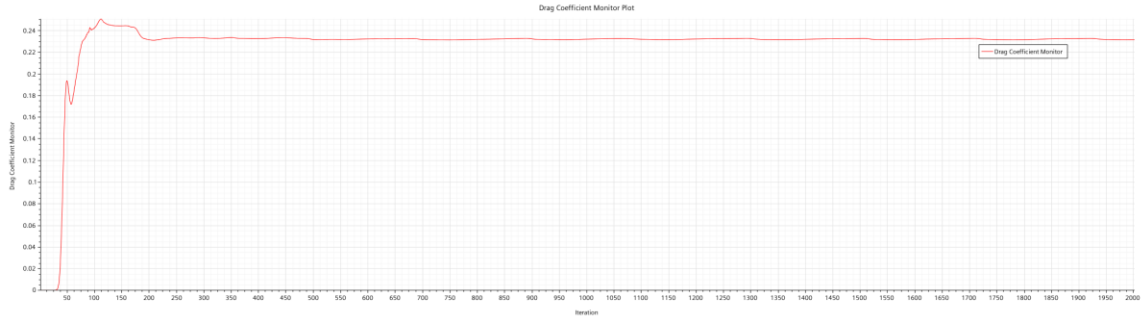
Figure 74: Drag Coefficient at α= 5°
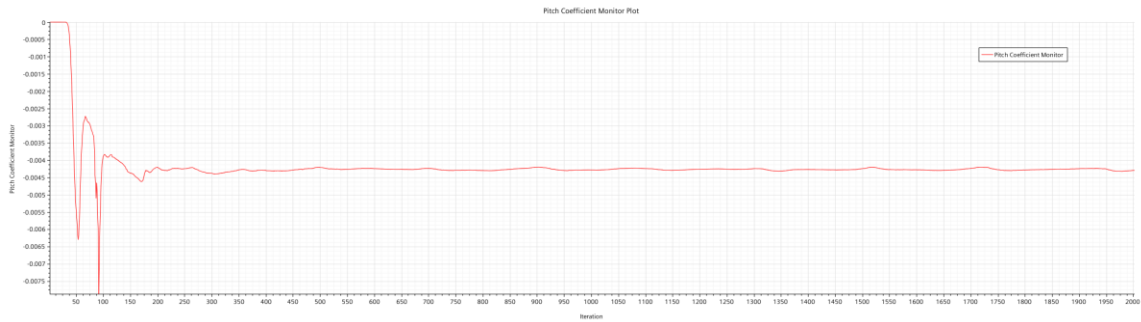
Figure 75: Pitch Moment Coefficient at α= 5°
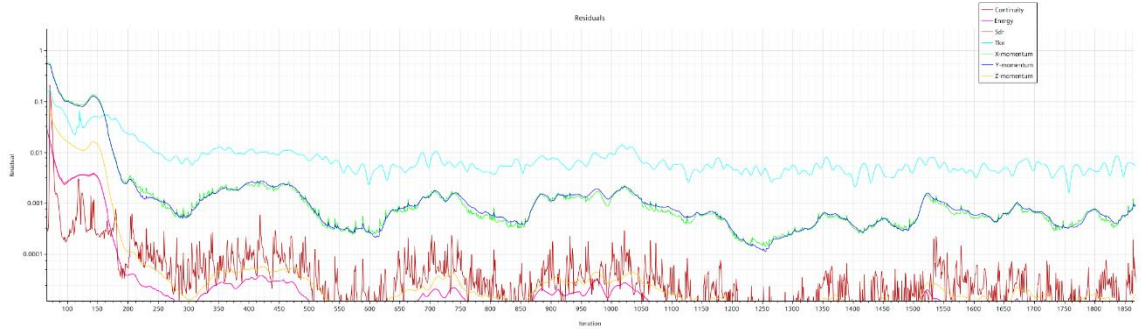
Figure 76: Residuals at α= 7.5°
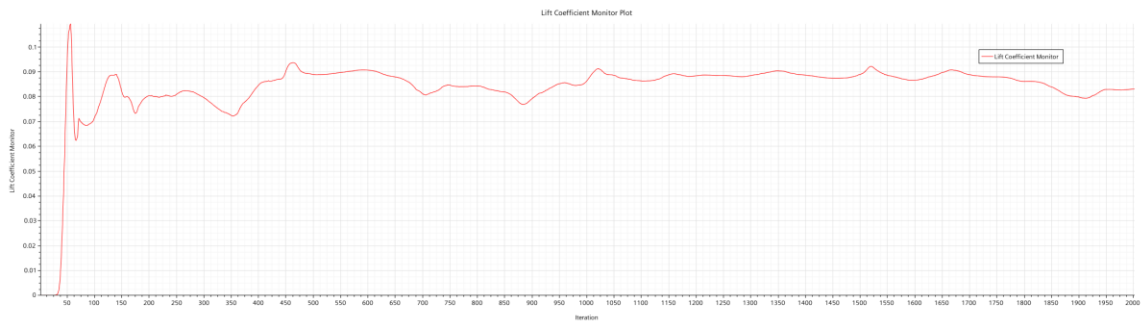
Figure 77: Lift Coefficient at α= 7.5°
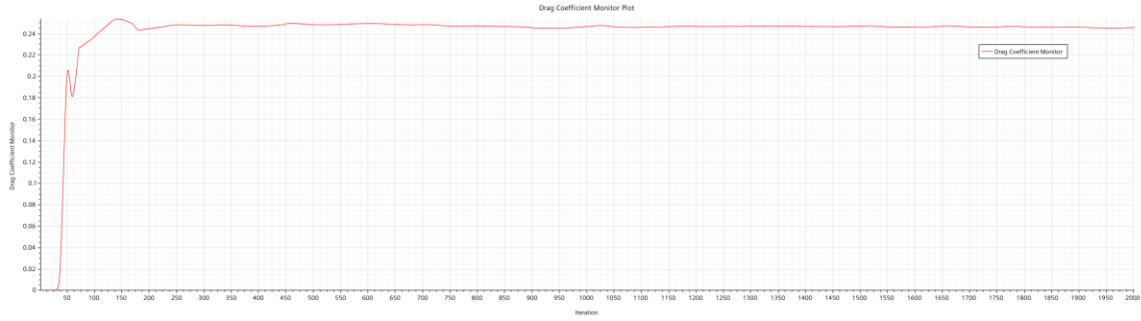
Figure 78: Drag Coefficient at α= 7.5°
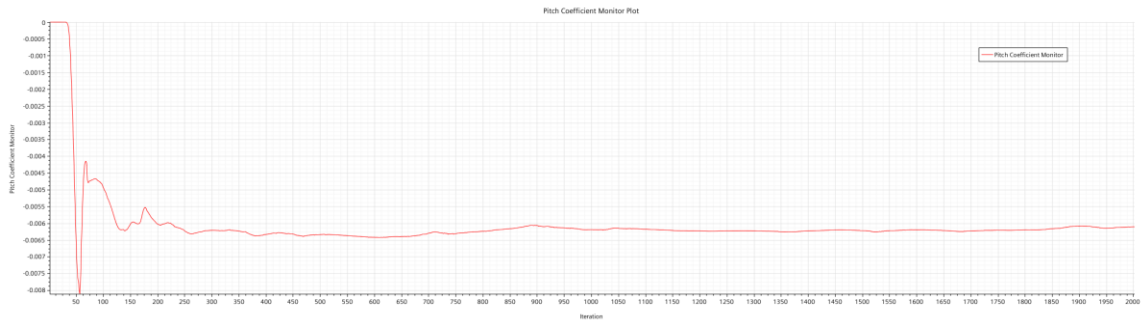
Figure 79: Pitch Moment Coefficient at α= 7.5°
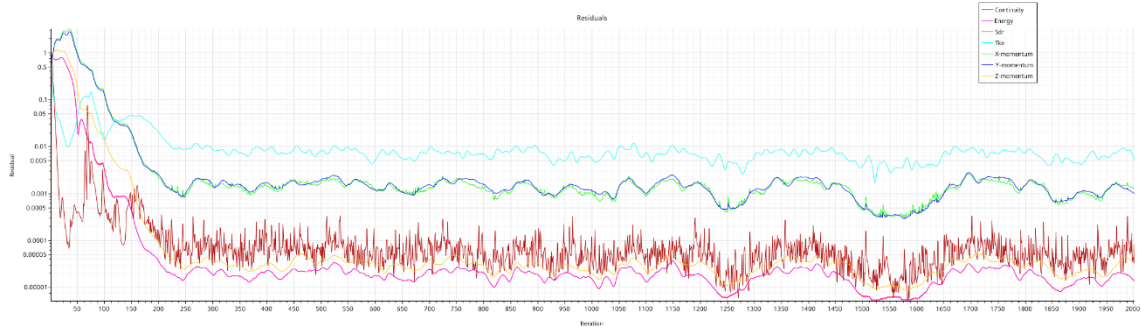
Figure 80: Residuals at α= 10°
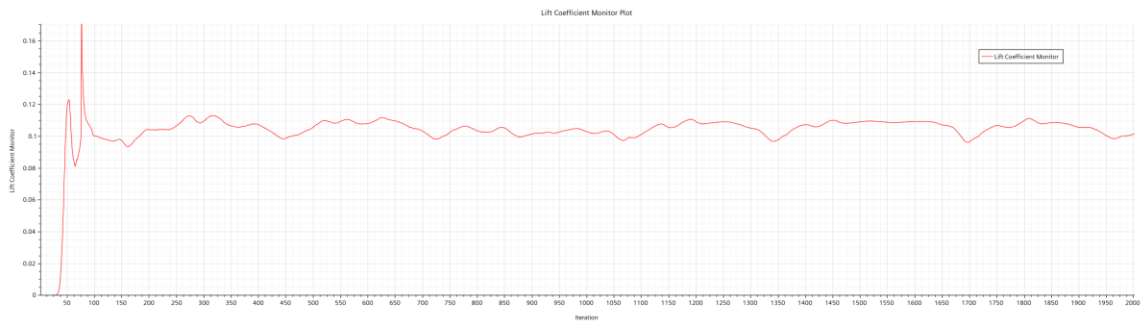
Figure 81: Lift Coefficient at α= 10°

56
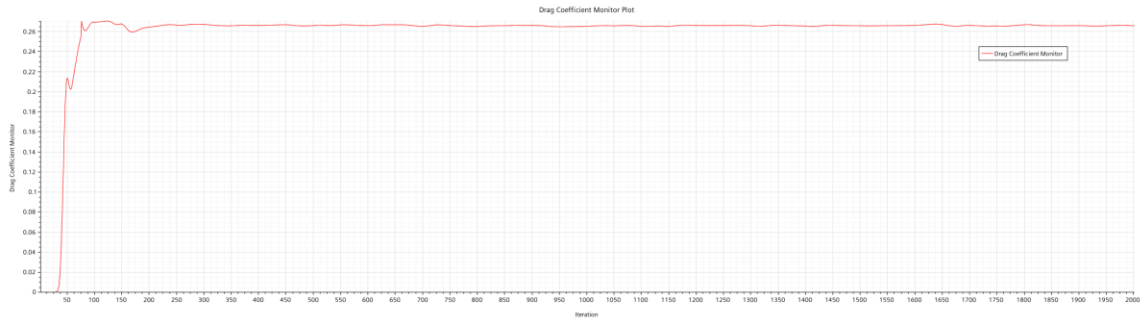
Figure 82: Drag Coefficient at α= 10°
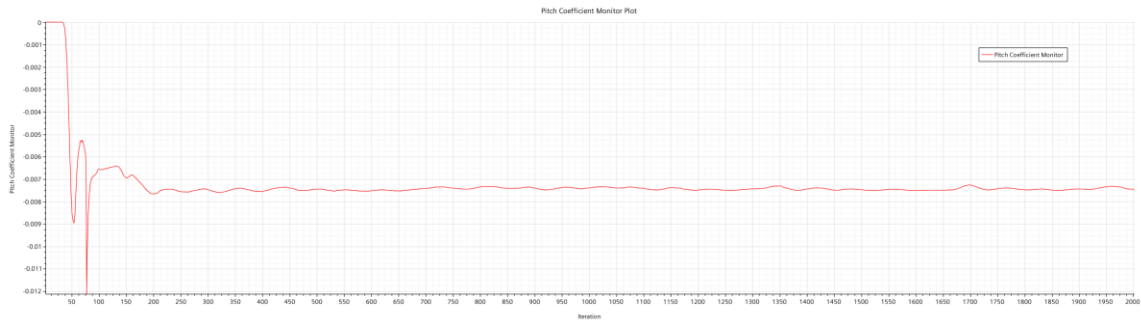
Figure 83: Pitch Moment Coefficient at α= 10°
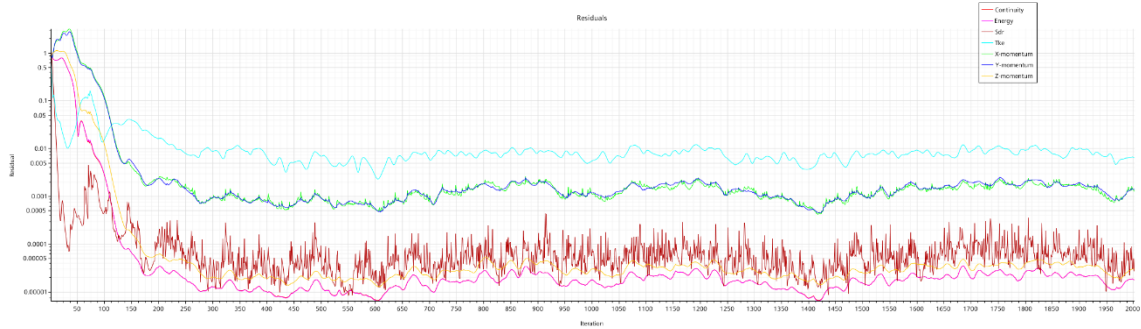
Figure 84: Residuals at α= 12.5°
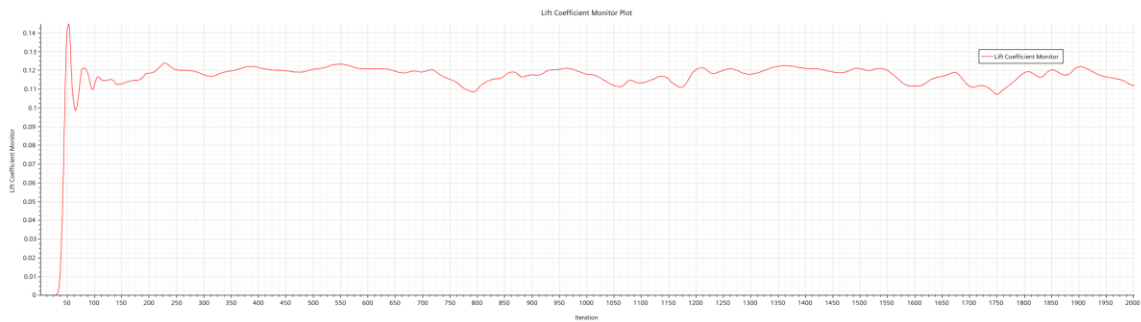
Figure 85: Lift Coefficient at α= 12.5°

57
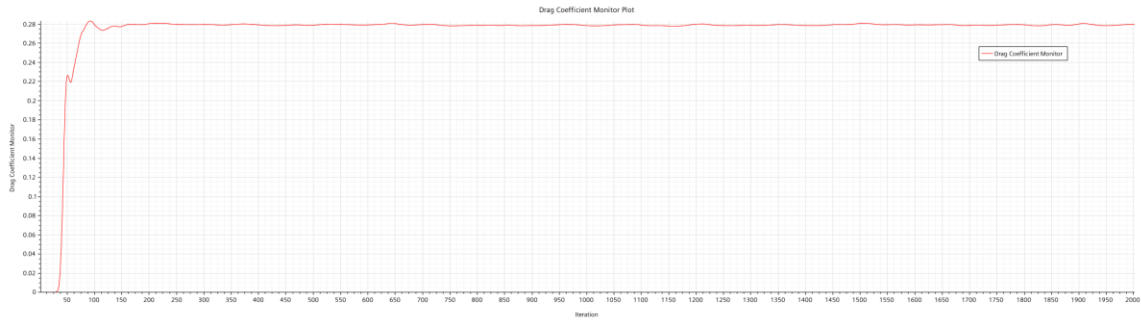
Figure 86: Drag Coefficient at α= 12.5°
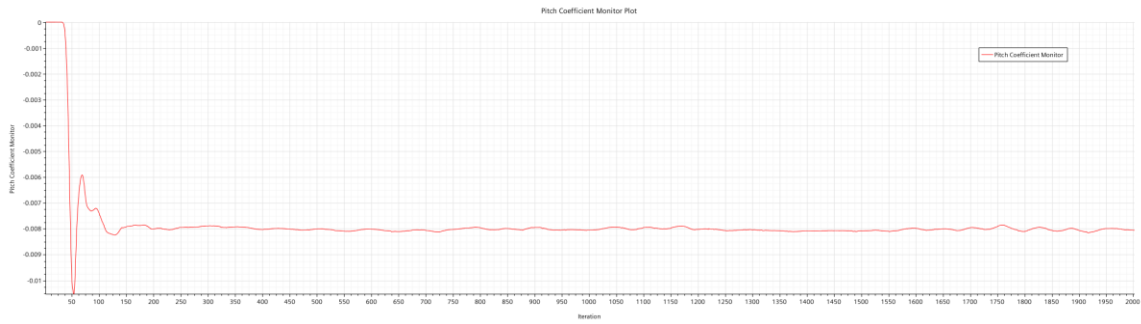
Figure 87: Pitch Moment Coefficient at α= 12.5°
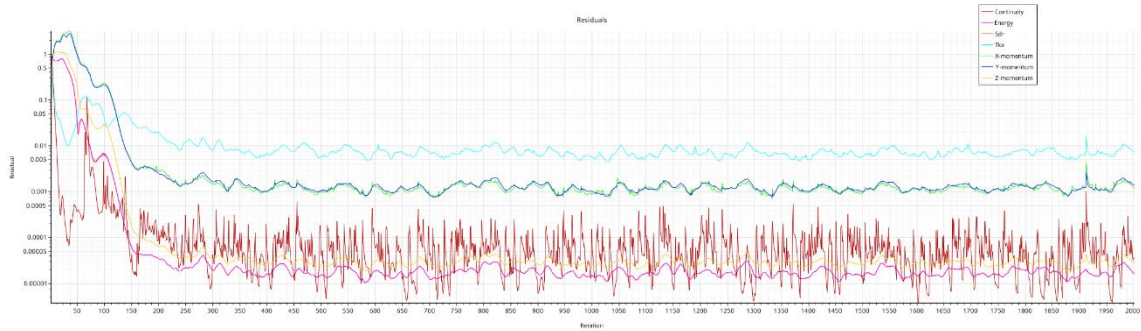
Figure 88: Residuals at α= 15°
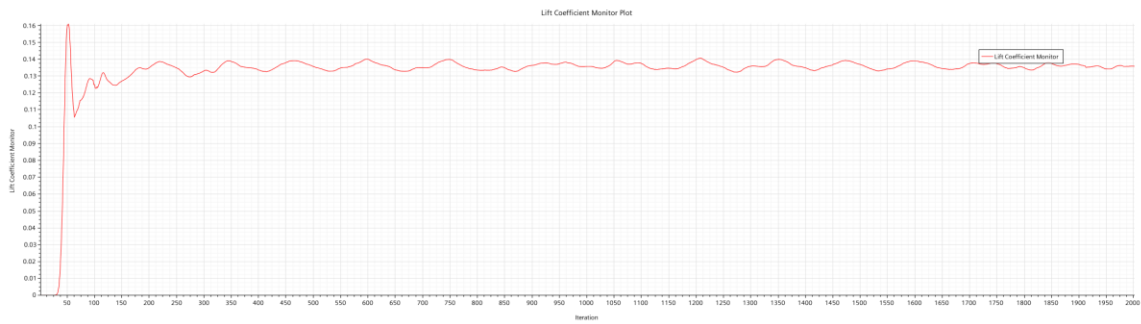
Figure 89: Lift Coefficient at α= 15°

58
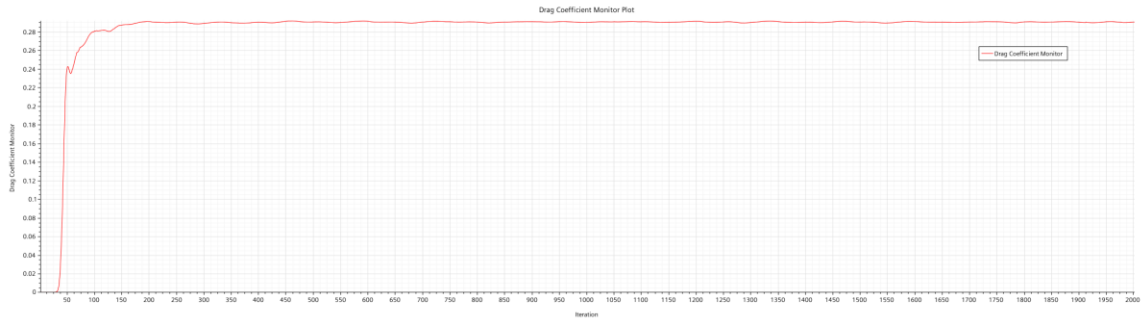
Figure 90: Drag Coefficient at α= 15°
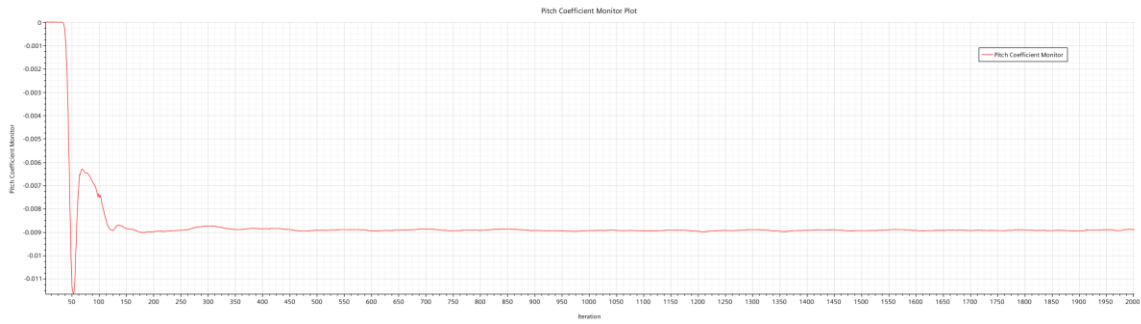
Figure 91: Pitch Moment Coefficient at α= 15°
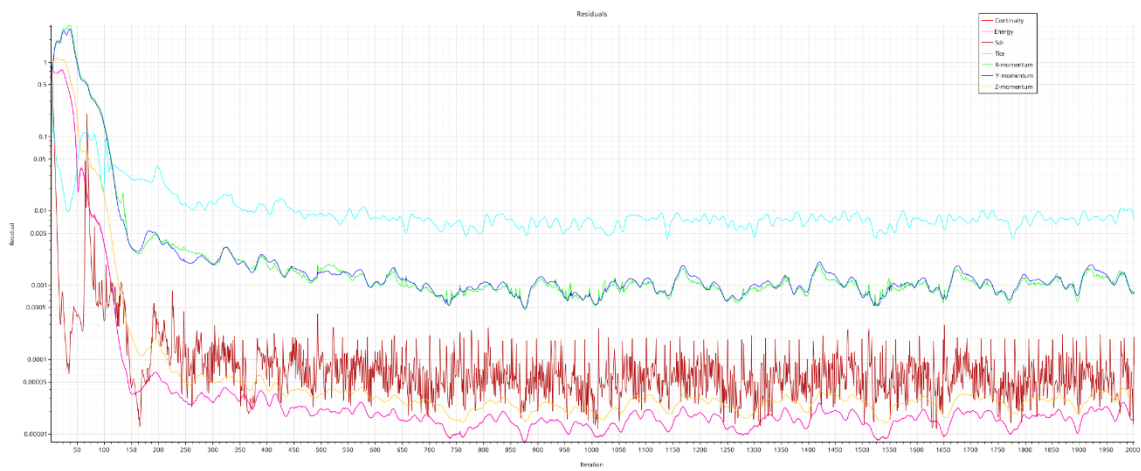
Figure 92: Residuals at α= 17.5°
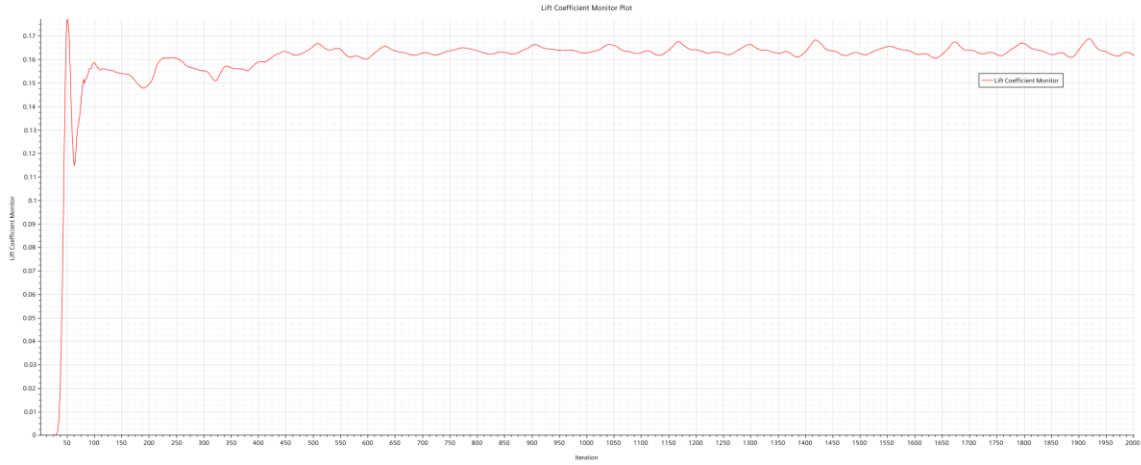
Figure 93: Lift Coefficient at α= 17.5°
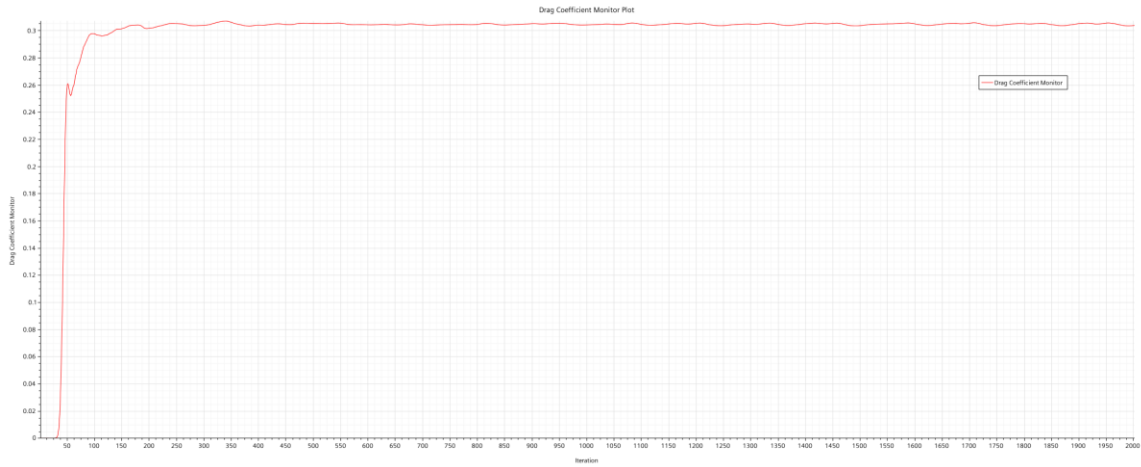
Figure 94: Drag Coefficient at α= 17.5°
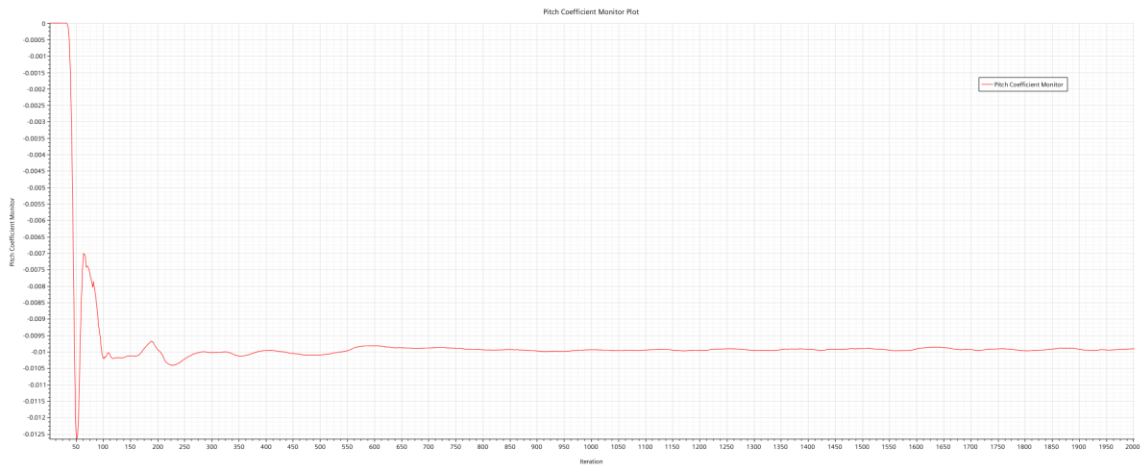
Figure 95: Pitch Moment Coefficient at α= 17.5°
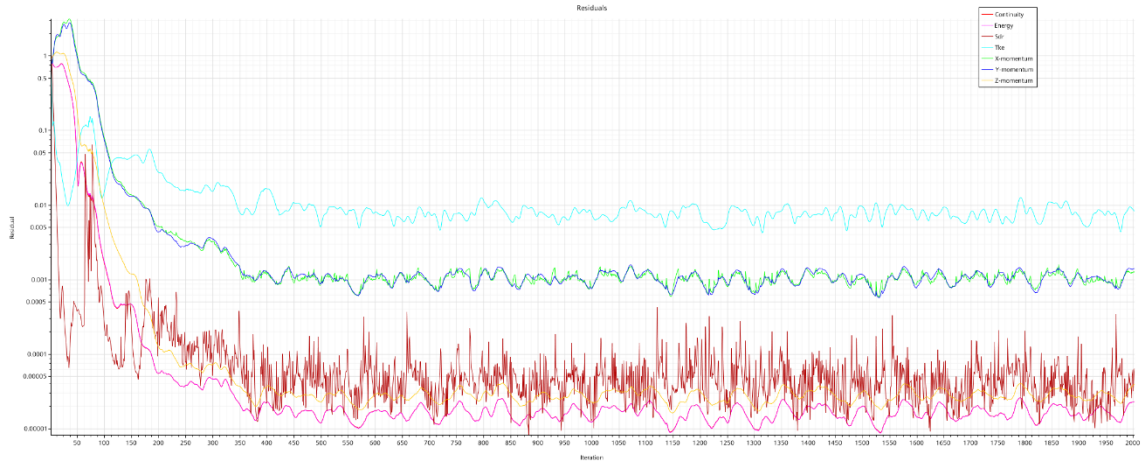
Figure 96: Residuals at α= 20°
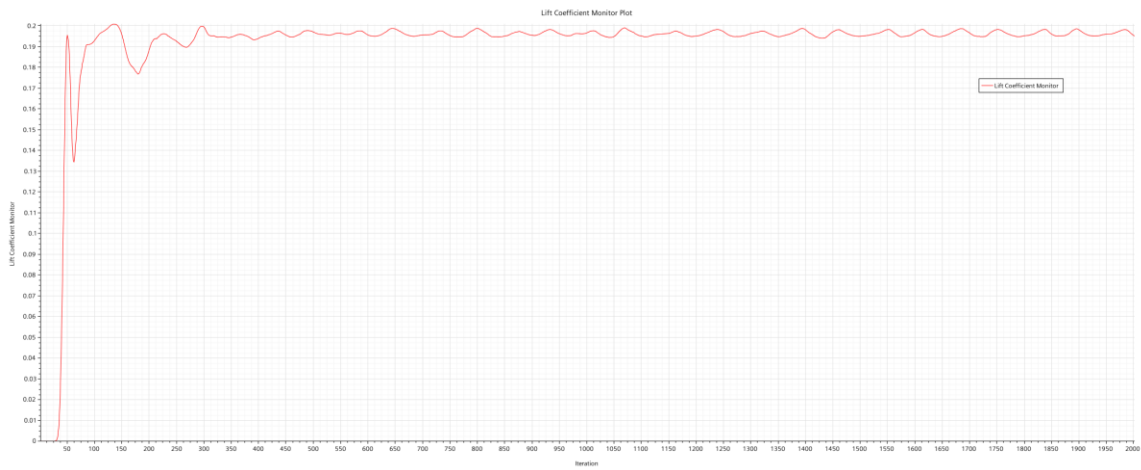
Figure 97: Lift Coefficient at α= 20°

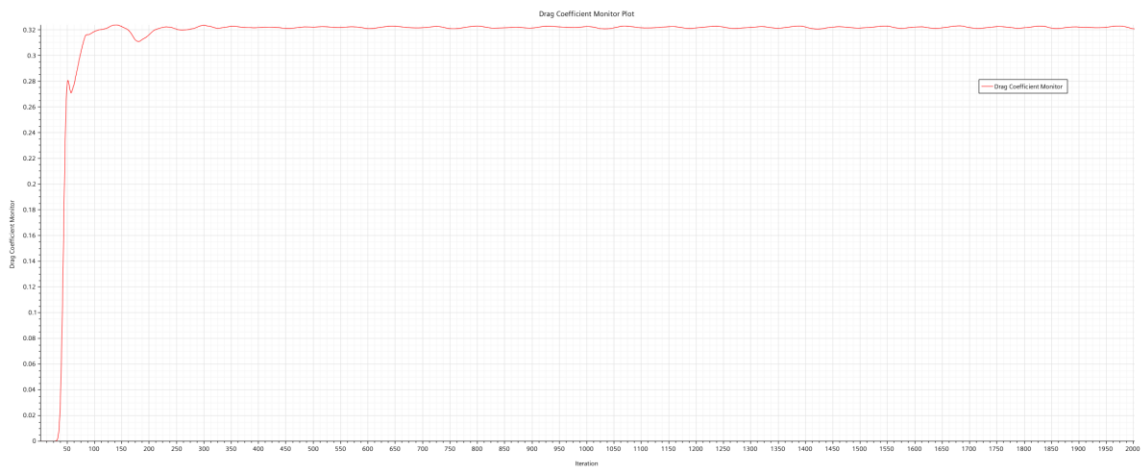*Figure 98: Drag Coefficient at α= 20°*

61

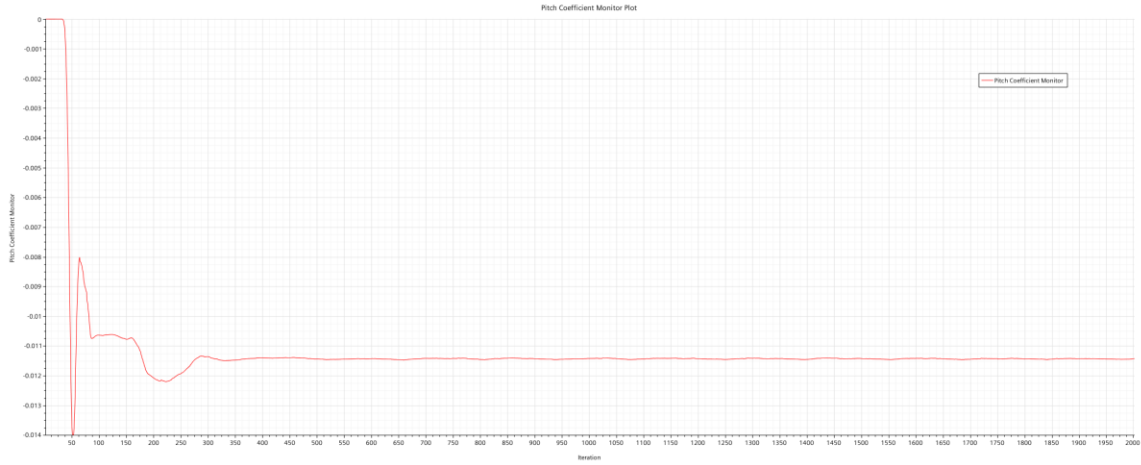*Figure 99: Pitch Moment Coefficient at α= 20°*

VITA

Christopher Daniel Totty

Candidate for the Degree of

Master of Science

Thesis: COMPUTATIONAL FLUID DYNAMICS STUDY FOR STABILITY ANALYSIS OF AN UNMANNED AIRCRAFT MASS SIMULATOR WITH ROCKET-ASSISTED TAKE-OFF

Major Field: Mechanical and Aerospace Engineering

Biographical:

Education:

Completed the requirements for the Master of Science in Mechanical and Aerospace Engineering at Oklahoma State University, Stillwater, Oklahoma in May, 2022.

Completed the requirements for the Bachelor of Science in Mechanical Engineering at Oklahoma State University, Stillwater, Oklahoma in 2019.

Completed the requirements for the Bachelor of Science in Aerospace Engineering at Oklahoma State University, Stillwater, Oklahoma in 2019.

Experience:

Graduate Research Assistant, Oklahoma State University, 2019-2022

Graduate Teaching Assistant, Oklahoma State University, 2019-2022

Aerospace Engineering Intern, RPX Technologies, Summer 2019

Undergraduate Research Assistant, Oklahoma State University, 2017-2019

Professional Memberships:

Tau Beta Pi, Sigma Gamma Tau, Pi Tau Sigma, American Institute of Aeronautics and Astronautics, American Society of Mechanical Engineers, Oklahoma Society of Professional Engineers